Surface Characterization of Textured Al Foil for Thin Film Flexible Solar Cells

Chinmaya Rath

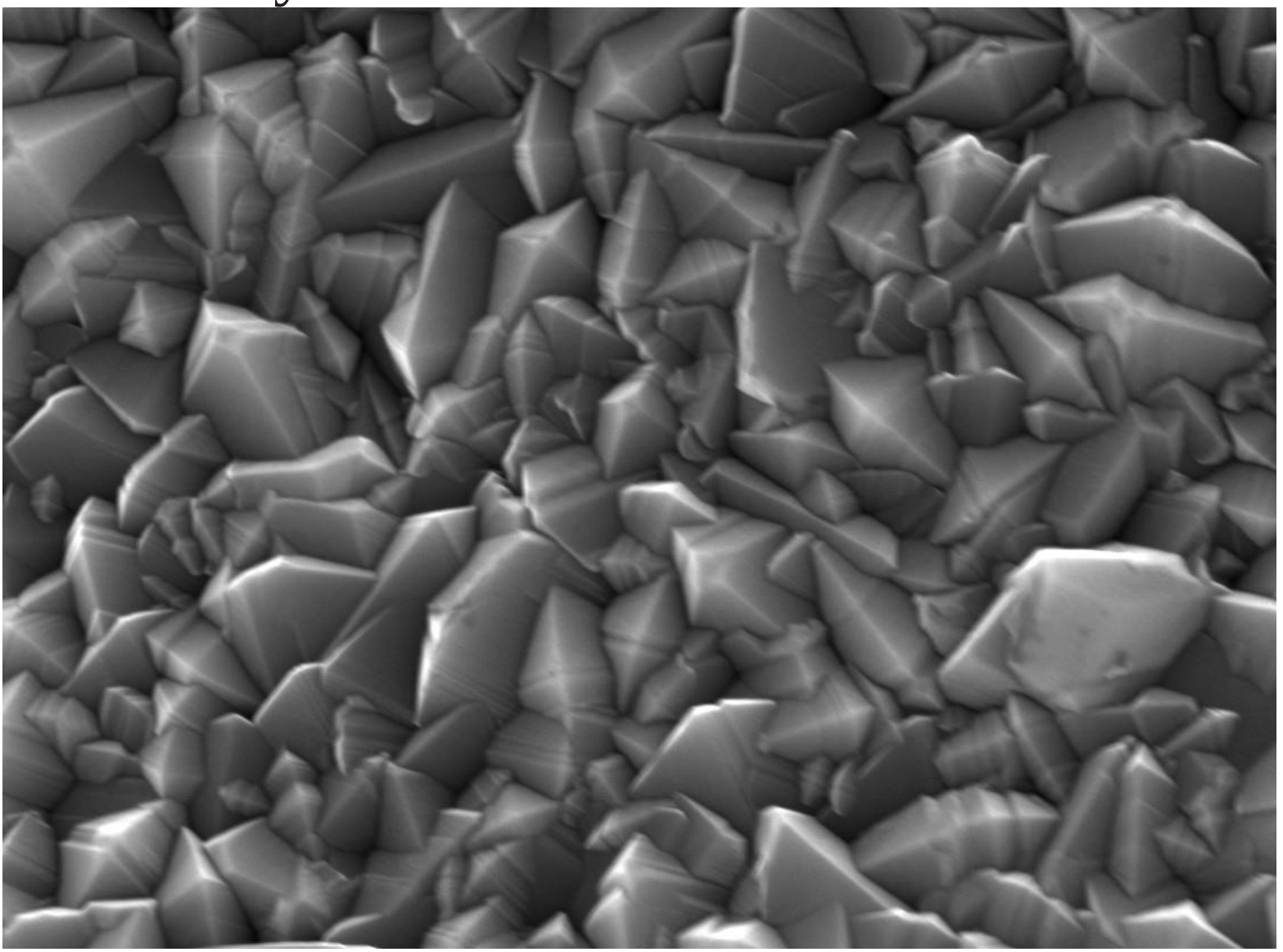

Surface Characterization of Textured Al Foil for Thin Film Flexible Solar Cells

FLAMINGO PV Project

by

Chinmaya Rath

In partial fulfilment of the requirements for the Master of Science degree
in Sustainable Energy Technology,
at the Delft University of Technology,
to be defended publicly on Monday March 7^{th,} 2022, at 3:00 PM.

Student number: 4806085

Thesis committee:

Prof. dr. A. H. M. Smets	TU Delft, ESE- PVMD, Supervisor
Dr. ir. R. Santbergen	TU Delft, ESE- PVMD, Assistant Professor
Dr. ir. A. Shekhar	TU Delft , ESE-DCES, Assistant Professor
Dr. G. Limodio	TU Delft, ESE-PVMD, Daily Supervisor
M. E. Makkaoui	HyET Solar, Daily Supervisor

Table of Contents

List of Figures

List of Tables

Acknowledgments:

Writing this thesis was one of the most amazing and learning experiences of my Master's program. It has been a wonderful time spent working in the labs and with a lot of people who made the journey a lot easier.

Dr. Gianluca Limodio, for being there every step to help and providing guidance whenever necessary. You were one of the best people to work with and the great support you provided throughout the journey wouldn't have been possible. This time you are the real boss.

Prof. Dr. Arno Smets, thank you for providing me the opportunity to work in the FLAMINGO PV group. You have been the inspiration and motivation for many in the field of PV technology and that includes me as well. Your kind words and positive outlook helped me a lot along with your valuable guidance and support.

My humble gratitude to Mr. Mohammed El Makkaoui for all your help in understanding the work done at HyET solar and implementing them at TU Delft. Also, for being available for discussion late and clearing my queries.

I would like to thank Dr. Thierry de Vrijer for his support in understanding AFM and doing the calculations relating to it and Prof. Dr. J. Van Wingerden for his help in understanding the equipment's in the lab.

Finally, a big thank you to my family and friends for their support and love throughout this journey. This has been an experience of a lifetime.

Chinmaya Rath

Delft, March 2022

Abstract:

With an increase in population, there is increasing pressure and higher demand in world energy production. Even though there is a high dependency on fossil fuels renewable energy usage has seen a sharp rise in recent years. Solar energy is a major player and contributes a lot to this field. The thin-film solar cell which is a part of second-generation photovoltaic technology is faster and easier to manufacture. What makes them even more desirable is that they are lightweight, cost-effective, and can be manufactured by roll-to-roll production. The transparent conductive oxide layer acts as a front contact for a solar cell and thus plays a major role in guiding the incident light towards the active layer. This TCO has to be deposited on the aluminium foil to utilize its high conductivity and transparency in the active wavelength.

This thesis is part of the FLAMINGO PV (Flexible Lightweight Advanced Materials in Next Generation of Photovoltaics) project with collaboration between HyET Solar B.V and TU Delft. Aluminium foil is used by HyET solar as a substrate for TCO deposition. The bare aluminium foil has high roughness values and imperfections due to the presence of milling tracks and pinholes. The objective of the thesis is to do structural and optoelectrical characterization on this substrate foil and TCO using different process methods.

Bare aluminium foil received by HyET solar which was pre-treated showed a higher roughness value when compared with the untreated samples. This also provided good correlation data with one of the supplier companies. Morphological analysis showed 2020 factory baseline samples having more milling tracks and pinholes compared to 2021 factory baseline samples. The pre-treated sample showed the presence of precipitants which was not the case in untreated samples. FLAM02 textured aluminium foils showed higher roughness values when compared to the 2020 and 2021 factory baseline but this has an overall better impact on its optical property. For Al + TCO samples structural characterization showed the presence of milling tracks and pinholes. Using a scanning electron microscope, the optical thickness of TCO was confirmed. For TCO + Carrier foil fewer milling tracks were noticed while characterizing them with SEM and 3D confocal microscope.

Optical characterization for the textured sample shows a similar value in diffused reflectance between the 2020 and 2021 factory baseline and a small increase in specular reflectance for 2020 factory baseline samples. FLAM02 textured samples showed a higher value in diffused reflectance and haze as compared to factory baseline 2021 and FLAM01 textured samples. Electrical characterization done on TCO + Carrier foil where a low free carrier concentration and high mobility is desired.

1

Introduction

Sustainable energy is the energy that meets the necessity of present generations without compromising the ability of future generations to meet their own needs. The main goal is to find clean energy that is a renewable energy source that replenishes itself rather than the sources that get depleted like coal and natural gas [1]. The demand for renewable increase lead to a 3% increase in its use in 2020. A major driver for this was an increase in electricity generation from renewable energy by 7%. For the year 2021 electricity generation from renewable energy is set to increase by 8% and to reach a total of 8300 TWh which is the fastest growth since 1970. The major contributors are solar PV and wind which account for two-thirds of the growth as seen in 1.1 below [2].

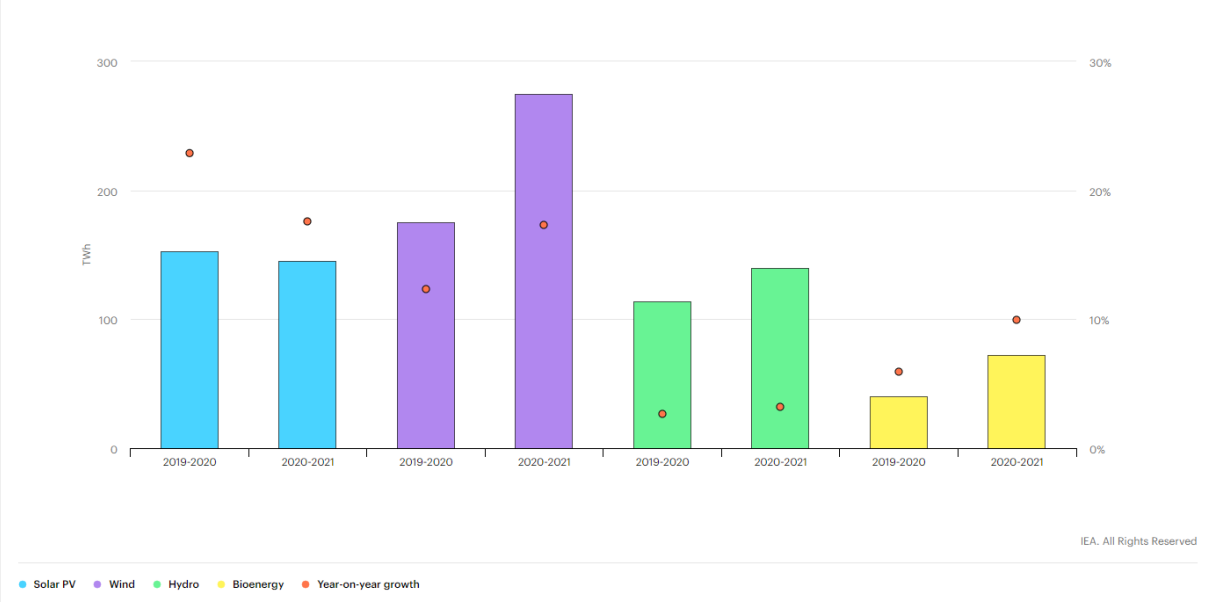

Figure 1. 1: Renewable energy electricity generation increase [2].

The conversion of sunlight into usable energy form is called solar energy. Various technologies like solar photovoltaics (PV), solar thermal electricity, and solar heating and cooling are well established. Solar PV has combined two major advantages: manufacturing of the module can be done in large plants which allows for economies of scale, and it is a modular technology that can be deployed in small quantities at a time [3]. From the year 2000, the global cumulative solar PV capacity has seen growth. From figure 1.2 below we can see that the global cumulative solar PV capacity valued to be 773.2 GW with an addition of 138 GW of new PV capacity was installed in 2020 [4].

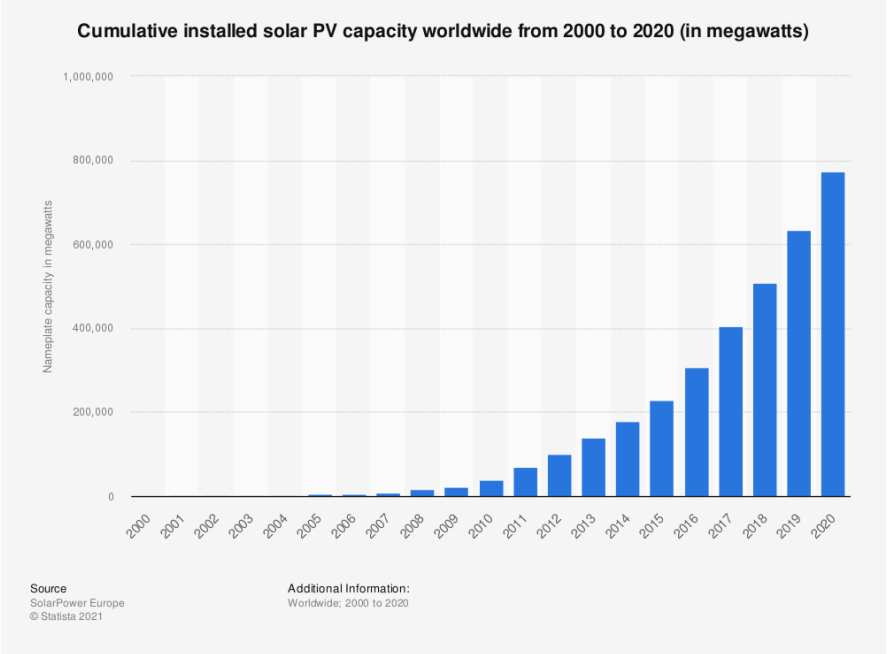

Figure 1. 2: Cumulative installed solar PV capacity worldwide from 2000 to 2020 [4].

1.1. Thin-film solar cells:

Thin-film solar cells are a part of second-generation solar cells which are made on a glass, plastic, or metal substrate by employing a single or multiple thin layers of PV elements [5]. The three most widely commercialized thin-film solar cell types are amorphous silicon(a-Si), cadmium telluride (CdTe), and copper indium gallium selenide (CIGS). The three materials used here have a direct bandgap which allows the use of thin materials [6].

Thin-film solar cells are the easiest and fastest solar panel type to manufacture. These types of solar panels have three main parts: a photovoltaic material like a-Si, CdTe, or CIGS; a layer of conducting material like aluminium to improve conductivity and prevent electricity loss; a protective layer such as high-quality glass or plastic I added to improve durability [7].

The major advantage of using thin-film solar cells over crystalline silicon cells which are wafer-based would be a reduction in cost due to the use of less silicon which leads to faster payback time. Also, there would be a higher output as thin-film-based silicon cells can be produced by roll-to-roll technologies. Compared to other thin-film technologies, silicon-based thin-film technology has the most industrial growth as well [8]. Even though we see these major advantages, thin-film PV has seen a decrease in market share from having 19% in 2009 to just having 8% in 2014 [9]. The factors that are contributing to these trends would be a decrease in crystalline silicon cost and an increase in efficiency of the crystalline silicon market. On the other hand, thin-film technologies are facing challenges in achieving stable efficiency and complexity in their production process [10].

Although there are several manufacturing technologies implemented in the production of thin-film solar cells, roll-to-roll production has several advantages like high throughput fabrication and having a flexible and lightweight product [11]. With the serial interconnection of cells and efficient deposition in the substrate configuration, the cost of production can be reduced as well [12].

1.2. FlamingoPV and Hyet Solar:

This thesis work is developed as a part of the FlamingoPV project which is also known as *Flexible Lightweight Advanced Materials In Next Generation of PV*. It is a collaboration between the Delft University of Technology and HyET Solar which is a subsidiary of HyET Group. The company is based in Arnhem, The Netherlands which aims to achieve low-cost, lightweight, and flexible solar modules with a high energy yield. The project aims to develop PV modules having efficiencies greater than 12% and a lifetime greater than 35 years.

HyET Solar uses a roll-to-roll manufacturing process which is used for making temporary Aluminium foil substrate [13]. In this, a lightweight flexible polymer is used to encapsulate thin-film amorphous silicon and microcrystalline silicon cells which increases their lifetime. This results in the production of modules of thickness under 0.5mm and a surface density of 0.6kg/m^2. This overall leads to an energy payback time of less than a year and the production of modules using only abundant and non-toxic materials [14].

FlamingoPV project comprises the following deliverables [15]:

1. Lab-scale flexible amorphous silicon/microcrystalline silicon tandem cell (5 cm^2) and module (5x5 cm^2) with a stabilized efficiency of 13%.
2. Production of roll-to-roll modules of dimensions 30x30 cm^2 with 12% aperture area stabilized efficiency and 80% production yield.
3. The operating lifetime of modules is more than 35 years while continuing performance above 80% of the initial value.
4. Design a PECVD tool for the bottom cell with a capital expenditure of less than 0.2 €/W_p.
5. Lab-scale flexible triple junction a-Si:H / nc-Si:H / nc-Si:H cells (5 cm^2) and modules (5x5 cm^2) with stabilized efficiencies equalling 14%.

These deliverables when achieved will result in thin-film modules which can provide competition to crystalline silicon modules-based market and be used for higher power production.

1.3. Roll-to-roll (R2R) Processing Method:

The roll-to-roll production technique used by HyET solar uses an aluminium substrate that is etched away in the further process, so the transparency requirement of the substrate foil is not needed. This technology was developed by the Helianthos consortium in the year 1997 along with Akzo Nobel, Delft University of Technology, Utrecht University, and TNO [16]. The company was then taken over by HyET solar for further development. As the aluminium foil used here is etched away this allows superstrate configuration although the substrate material used is not transparent.

The R2R processing method used by HyET solar goes through eight steps as depicted in figure 1.3. In step 1, as aluminium foil can withstand high temperatures, the front TCO is deposited by atmospheric pressure chemical vapor deposition (APCVD) at temperatures ranging between 500^{o}C and 550 ^{o}C. This allows a higher deposition rate of 100 nm/s and a uniform deposition. Fluorine doped tin oxide (SnO_2:F) has a higher resistance to corrosion from moisture and acid so it is the preferred TCO over aluminium doped zinc oxide (ZnO:Al). After this layer of TCO, the p-i-n silicon layer is deposited as superstrate using RF Plasma Enhanced Chemical Vapour Deposition (PECVD).

In step 2, laser scribing is done to define the cell areas which are then labeled as P1s and P2s. To insulate the active layer in step 3, a TCO-filled ink is inserted at P1s. For step 4, a lift-off ink is injected at P3f which aims to decrease the number of laser scribes in the process. In step 5, the back contact which has aluminium doped zinc oxide and aluminium (AZO:Al) are sputtered in a DC magnetron sputtering. In step 6, for isolation of the back contact, the filler ink is removed. In step 7 using an adhesive and a mechanical press, the carrier foil is laminated to the back contact after which wet chemical etching is done to the temporary Al foil substrate. In step 8 polymer encapsulation is made at the top and a busbar is incorporated to make an electrical path that gives the final product [17].

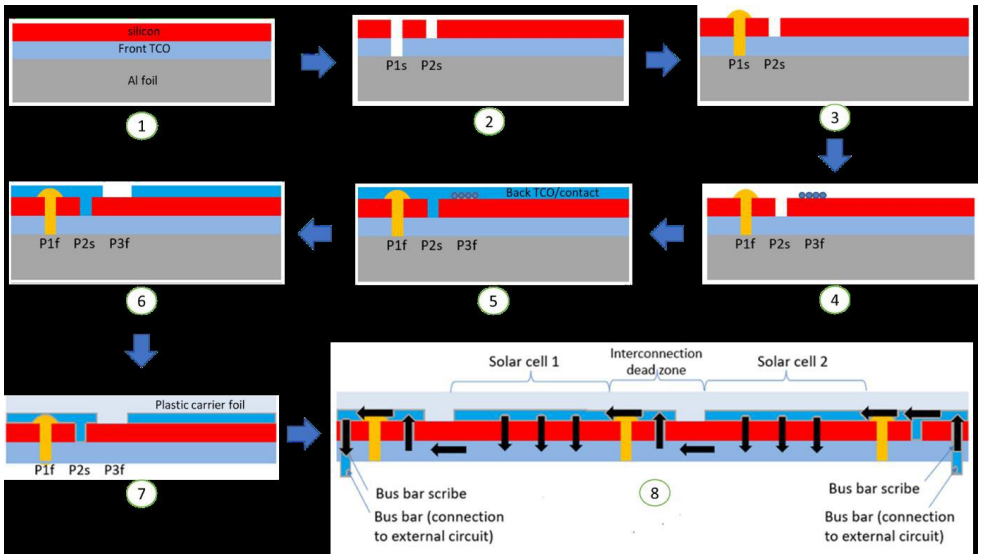

Figure 1. 3: Steps involved in roll-to-roll processing used by HyET solar [17].

1.4. Aim and Outline of the Thesis:

This thesis is a part of the FlamingoPV project with the goal of TCO analysis and characterization. The features of the front window layer are of crucial importance to improve the efficiency of thin-film flexible silicon solar cells. For this thesis, we understand the properties of such TCO layers which are to be embedded inside the solar cells. Optical and morphological features are investigated and analyzed using different methods.

Foil received by HyET solar has issues that can be divided into two categories :

a) Received foil has pinholes, milling tracks, and scratches which causes problems in TCO like cracks.
b) Issues inherent to the process undertaken by HyET solar-like pre-treatment of the foil surface.

The primary objectives of this thesis are:

a) Doing morphological characterization using 3D Confocal Microscope and SEM for:
    - Aluminium foils received by HyET solar
    - Textured aluminium foils after pre-treatment
    - Aluminium foil deposited with TCO
    - FLAM02 textured aluminium foil
    - TCO deposited on carrier foil

b) Morphological characterization using AFM to check the structural properties of the FLAM02 texture

c) Optical characterization using Integrating sphere for reflectance and transmittance for:
    - Aluminium foil deposited with TCO
    - FLAM02 textured aluminium foil
    - TCO deposited on carrier foil

d) Electrical characterization using Hall Effect Measurement for:

    - TCO deposited on carrier foil

.

2

Fundamental Concepts

2.1. Solar cell working :

The basic principle on which solar cells work is based on the photovoltaic effect. It states that the potential difference generated at the junction of two different materials is in response to electromagnetic radiation. This effect was understood by *Albert Einstein* in 1905, which can be explained by the assumption that light has well-defined energy quanta, known as photons [18].

The energy from such a photon is given by the equation:

$$E = h\nu \qquad (2.1)$$

Where, h = Planck's constant ;

ν = speed of light.

The photovoltaic effect is divided into three basic steps :

a) Generation of charge carriers due to photon absorption resulting in junction formation: When a photon is absorbed in a material its energy excites an electron from initial energy level E_i to a higher energy level E_f. Photons will be absorbed only if the two energy levels E_i and E_f are present as their difference will give us the photon energy which is, $h\nu = E_f - E_i$. If we consider an ideal semiconductor, electrons can occupy both levels below the valence band edge, E_v, and above conduction band edge, E_c. The energy difference between these two levels is called the bandgap where no allowed energy states exist which can be occupied by electrons. A void is created at the E_i when the electron is excited from E_i to E_f. This void is also known as a hole that behaves like a particle with a positive elementary charge. This process is illustrated in figure 2.1 below [18].

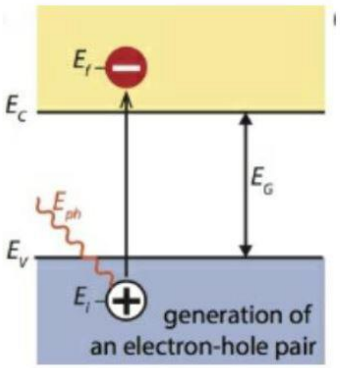

Figure 2. 1: Illustration of generation of an electron-hole pair

b) Separation of photo-generated charge carriers subsequently: As the electron-hole pair will combine resulting in the electron returning to the initial energy level E_i. This process results in energy release either as photons or is transferred to other electrons. To utilize this energy semipermeable membranes are needed on both sides such that electrons flow out through one side and holes through the other side. For solar cells, these semipermeable membranes are n- and p-type materials. Taking this into account solar cells are designed that the electrons and holes do not recombine and reach the membrane [18]. This process is illustrated in figure 2.2 below.

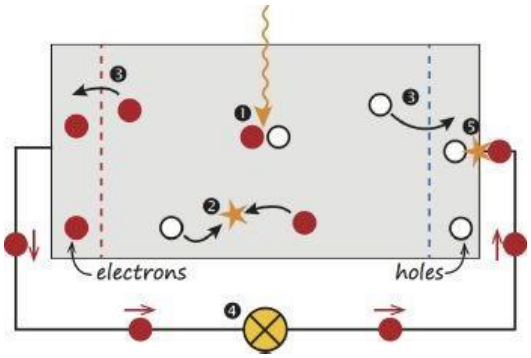

Figure 2. 2: A simple solar cell model.

c) Collection of photo-generated charge carriers at the junction terminal: Thus, the charge carriers are extracted from the solar cells with suitable electrical contact to perform work as shown in figure 2.2. Chemical energy obtained from the electron-hole pair is converted to electrical energy. Finally, after the electrons pass through the circuit they recombine with holes as shown in figure 2.2 [18].

2.2. Classification of solar cells:

The solar cell can be classified into four generations which is mainly based on the time and materials used for their fabrication [19].

a) First-generation solar cells: Due to their high efficiencies this is the most commonly used type and the oldest as well. They are produced on wafers and to increase their power solar modules having many cells are used. First-generation solar cells are divided into two types which are based on their crystallization levels. The first type is called single crystal solar cell as the whole wafer is one crystal. The second type is called multi-crystal solar cell as the wafer has crystal grains. Monocrystal solar cells have higher efficiency, but the production of multi-crystal solar cells is cheap and easy to make [20].

b) Second-generation solar cells: This generation of solar cells is primarily made of thin-film solar cells. Although their efficiencies are less than the first-generation modules, their cost of production is less as well. As they don't have any fingers for metallization, they have a wider application on building integration and windows. These thin-film materials can be made on a flexible substrate and as an added advantage they can be grown on larger areas up to 6 m^2. Various types of second-generation solar cells include Amorphous Silicon-based, Cadmium Telluride based and Copper Indium Gallium Selenide-based solar cells [20].

c) Third-generation solar cells: These types of solar cells include dye-sensitized solar cells and organic photovoltaics that use organic polymers and dyes. Their future growth includes the use of cheaper materials, roll-to-roll manufacturing, and greater power density. Third-generation solar cells are lightweight, flexible, and easy to integrate. They also have a low cost of production and long life [21].

d) Fourth-generation solar cells: This generation of solar cells falls in the class of conjectural generation consisting of composites. These are generally materials like hybrid in-organic crystal with polymer matrix [19].

2.3. Optics :

Optics deals with the properties of light and plays a major role in solar cells as sunlight is used for power generation. In this chapter, we discuss the properties of light like reflection and refraction and how light behaves in flat interface and absorptive media. When sunlight is incident in a solar panel it will absorb a portion of it which is used to generate electricity and the rest is reflected and scattered.

2.3.1. Optics of flat interfaces :

An electromagnetic wave is traveling between medium 1 and medium 2 is taken and it is assumed that these two media is non-absorptive. The real part of the refractive indices is taken and named as n_1 and n_2. When light travels through these media a part of the light is reflected where the angle of reflection Θ_r is equal to the angle of incidence Θ_i,

$$\Theta_r = \Theta_i \qquad (2.2)$$

The other part of the light is refracted when enters medium 2 as shown in figure 2.3. Thus, the angle of refraction Θ_t can be related to the angle of incidence Θ_i by Snell's law,

$$n_1 \sin\Theta_i = n_2 \sin\Theta_t \qquad (2.3)$$

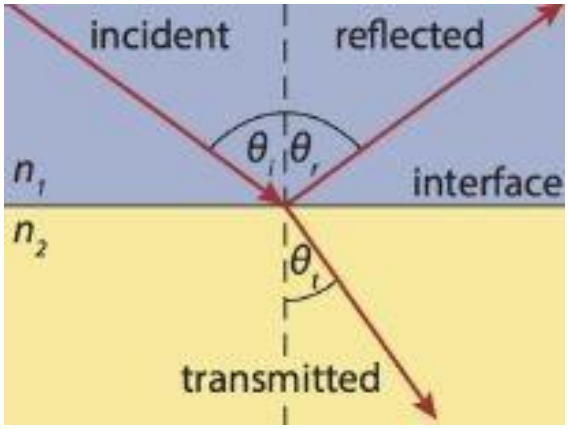

Figure 2. 3: Reflection and refraction of light

Finally, we take the magnitudes of refracted, reflected, and incident light, they can be linked by the Fresnel equation. The electric field can be parallel or perpendicular to the plane of incidence, which is dependent on the polarized light as well. For perpendicular polarized light, the Fresnel equations are given by:

$$t_s = \left(\frac{\xi_{0t}}{\xi_{0i}}\right)_s = \frac{2n_1 \cos\theta_i}{n_1 \cos\theta_i + n_2 \cos\theta_t} \qquad (2.4)$$

$$r_s = \left(\frac{\xi_{0r}}{\xi_{0i}}\right)_s = \frac{n_1 \cos\theta_i - n_2 \cos\theta_t}{n_1 \cos\theta_i + n_2 \cos\theta_t} \quad (2.5)$$

For parallel polarized light, the Fresnel equations are given by:

$$t_p = \left(\frac{\xi_{0t}}{\xi_{0i}}\right)_p = \frac{2n_1 \cos\theta_i}{n_1 \cos\theta_t + n_2 \cos\theta_i} \quad (2.6)$$

$$r_p = \left(\frac{\xi_{0r}}{\xi_{0i}}\right)_p = \frac{n_1 \cos\theta_t - n_2 \cos\theta_i}{n_1 \cos\theta_t + n_2 \cos\theta_i} \quad (2.7)$$

While calculating the reflectivity R for the unpolarised light we have to take the mean value of both perpendicular and parallel polarization, which gives us:

$$R = \frac{1}{2}(r^2_s + r^2_p) \quad (2.8)$$

We also know that by the law of conservation of energy, the sum of reflectance and transmittance is equal to 1.

$$R + T = 1 \quad (2.9)$$

Thus, from equation 2.8 and 2.9 we get:

$$T = 1 - R = \frac{n_2 \cos\Theta_t}{n_1 \cos\Theta_i} \frac{1}{2}(t^2_s + t^2_s) \quad (2.10)$$

For normal incidence ($\Theta_i = 0$); So;

$$T = \frac{4 n_1 n_2}{(n_1 + n_2)^2} \quad (2.11)$$

From Snell's law if we consider total reflection then $n_1 > n_2$ and because of critical angle light cannot leave the layer with n_2 [18],

$$\sin\Theta_{crit} = \frac{n_1}{n_2} \quad (2.12)$$

This phenomenon is taken into account while designing a solar cell to capture light using texturing.

2.3.2. Optics in absorptive media:

An absorber material absorbs light and excites charge carriers which can be used to run an electric circuit, this is the basic working principle of a solar cell. The optical properties of an absorbing medium are explained by a complex electric permittivity $\tilde{\varepsilon}$,

$$\tilde{\varepsilon} = \varepsilon' + i\,\varepsilon'' \tag{2.13}$$

Now we have an index of refraction $\tilde{n}$ which is a complex number as it is the square root of electric permittivity ($\sqrt{\tilde{\varepsilon}}$),

$$\tilde{n} = \sqrt{\tilde{\varepsilon}} = n + ik \tag{2.14}$$

Lambert-Beer can be used to find the attenuation of the intensity of the electromagnetic field

$$I(z) = I_0 \exp(-2k_z'' z) = I_0 \exp(-\alpha z) \tag{2.15}$$

$$\text{Where } \alpha = 2\,k_z'' = 2\,\frac{k\omega}{c} = \frac{4\pi k}{\lambda_0}$$

Here α is called the absorption coefficient which is dependent on the wavelength. Then we have the penetration depth (δ_p) which is generally used to calculate the absorptivity of the material and is formulated as:

$$\delta_p = \frac{1}{\alpha} \tag{2.16}$$

Properties like complex refractive index and absorption coefficient vary with frequency. This makes the material very absorptive at one wavelength and pretty transparent at another wavelength [18].

2.4. Losses :

To understand how efficient a solar cell can be we analyze different building blocks. This is useful as it helps us understand why 100% of the energy incident on the solar cells cannot be converted to energy and we see the various efficiency limits.

2.4.1. The Thermodynamic Losses:

In this, the solar cell is compared to a thermodynamic heat engine that operated between a hot and a cold reservoir. This heat engine converts the energy in the heat of the absorber to an entropy less chemical energy which is stored like an electron-hole pair [18].

As the absorber gets heated as it absorbs sunlight. Ideally, it is assumed that the absorber to be a blackbody. In figure 2.4 below we see that the solar cell efficiency reaches a maximum of 85% when the absorber temperature is 2480 K. Although this model of the solar cell does not resemble a real solar cell but shows us the limitation of converting sunlight into electricity [18].

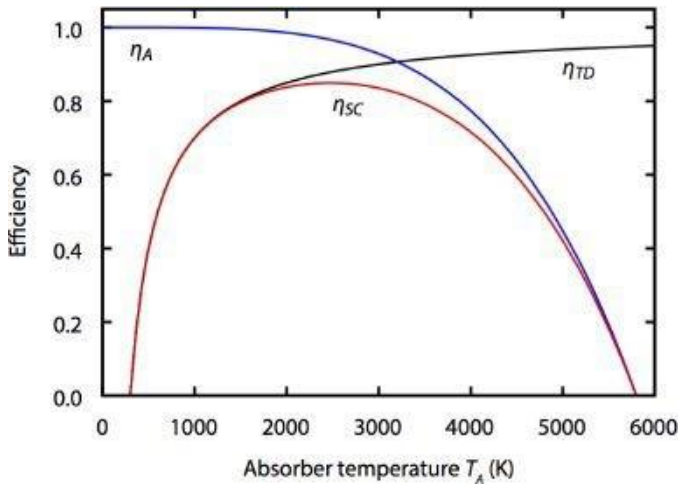

Figure 2. 4: The thermodynamic efficiency η_{TD}, absorber efficiency $\eta_{A,}$ and combined solar cell efficiency η_{SC} under the solar temperature of 5800 K and ambient temperature at 300 K [18].

2.4.2. Spectral Mismatch:

The theoretical limit of a single-junction solar cell is called Shockley-Queisser (SQ) limit. Here we discuss the spectral mismatch losses that belong to the SQ limit.

The absorber layer is an important part of the solar cell where electron-hole pairs are generated. Generally, the absorber layer is formed by a semiconductor material which is characterized by its bandgap energy. Photons having energy higher than the bandgap energy can make the electron-hole pairs. So, the photons not involved in the formation of the electron-hole pairs are called non-absorption photons and carry less energy than the bandgap. This with the photons having energy excess than the bandgap are the two main losses in the energy conversion process of the solar cells [18].

2.4.3. Optical Losses:

The performance of a solar cell is greatly affected by the optical properties as well which is represented by complex refractive index $\tilde{n}$ = n – ik, and is a function of wavelength. When light travels at the interface of two mediums a part of it is reflected and a part is transmitted. When multiple reflections and transmission occur at the various interfaces in a solar cell it results in a total internal reflection. Thus, a part of incident energy that could have been used by the solar cell is lost due to reflection [18].

If we take c-SI solar cells which use thin metal strips as front electrodes on the front side of the solar cells. This metal-covered part either reflects or absorbs the incident light and this decreases the active area of the solar cell. This loss is generally called shading loss. Light is absorbed in all layers of the solar cell and the absorption in layers other than the absorber layers is considered as a loss called parasitic absorption [18].

2.4.4. Additional Limiting Factors:

The other factors that play a role in losses and limits performance of a solar cell are:

a) Voltage drop occurs due to the series resistance of a solar cell, which is due to the resistance of the main current path.
b) Voltage drop due to leakage currents which is due to the shunt resistance of the solar cell.
c) There is a drop in the fill factor due to recombination in a non-ideal solar cell [18].

2.5. Texturing:

The Use of texturing helps us to improve the coupling of light into the layer by itself or in combination with anti-reflection coating [22]. As we see in figure 2.5 perpendicularly incident light may be reflected from one part of the textured surface to a second. In comparison to the flat interfaces here another part of the light will be transmitted into the layer and less light will be reflected [18]. Tandem solar cells manufactured by HyET solar show a higher level of internal stress on the nanocrystalline silicon so proper texturing is needed [23].

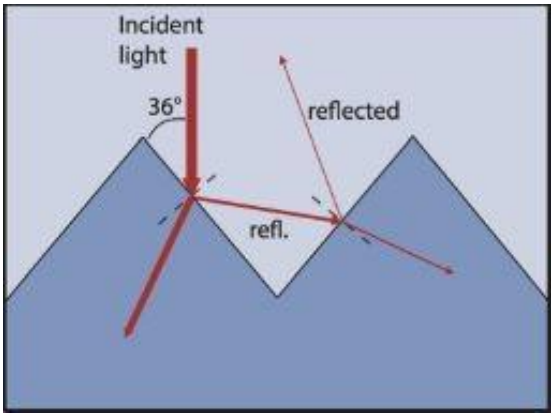

Figure 2. 5: Effect of texturing

2.5.1. Modulated Surface Texturing:

This type of texture can be used for a broad wavelength range. It is achieved by super positioning various scattering mechanisms by different geometrical features in a modulated surface texture. Combining suitable geometrical features and introducing them at the interfaces will help in achieving higher scattering in a wider wavelength range [24].

For thin-film silicon solar cells, it is still a challenge to design a light trapping mechanism that can trap light efficiently and help in the growth of a high-quality absorber layer for each of the sub-cell [25]. Taking an example of a-Si:H /nc-Si:H tandem solar cell we can see that the top a-Si:H junction has sharp textures to achieve light trapping thus a thinner absorber layer. The bottom nc-Si:H junction on the bottom has large and smooth textures [26][27]. Using sharp textures however reduces the electrical performance of nc-Si:H and a-Si:H by reducing the open-circuit voltage and fill factor [27][28]. The current choices are between having strong light trapping and growth of good quality silicon layer to better transparency and conductivity of the front electrodes constraining the improvement in efficiency [25].

Modulated surface texturing makes use of a combination of micro-sized and nano-sized features as shown in figure 2.6. The formation of cracks also is reduced by using micro-sized u-shaped craters. This finally results in fewer grain boundaries and voids by allowing the growth of crystals perpendicular to the relatively flat surface [17]. Due to MST substrates, there

is a high summed photocurrent compared to state-of-the-art LPCVD ZnO substrates in both tandem and triple-junction solar cells due to better transparency and light trapping [25].

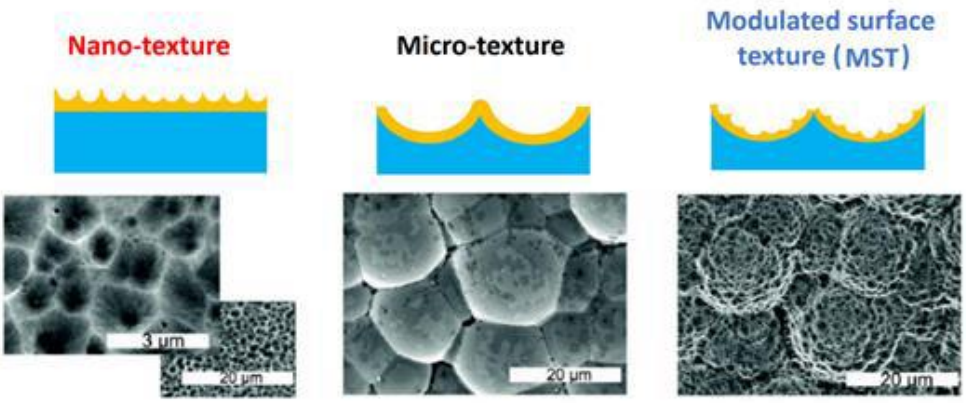

Figure 2. 6: Illustration showing combination of nano-texture and micro-texture for modulated surface textured features [17]

3

Experimental Methods

3.1. Scanning Electron Microscope (SEM) :

Hitachi Regulus 8230 features an ultra-high-resolution cold-field emission (CFE) SEM which is enhanced for sensitive material and nanostructures. Even below 1 Kv, there is sub-nanometer resolution available, and it uses a multi-detection system with energy filtering [29]. It allows resolution as low as 0.7 nm and is suitably optimized for high-resolution imaging at very low accelerating voltages. The CFE feature in this SEM allows it to magnify an image by 2 million times [30].

Figure 3. 1: Scanning Electron Microscope Regulus series by Hitachi

In SEM a stream of electrons is emitted from a source which is used to measure features in the range of nanometres that is smaller than the wavelength of light. Secondary electrons are produced when the electron stream directed by electromagnets bounce from the surface. These bounced off secondary electrons are then registered by a detector and turn into an image that we see on the screen [31]. During imaging, the sample is held in a vacuum through a holder in the chamber. Then by using the software user can take close-up images of the surface to micrometer and nanometer level. This also allows doing measurements of different features by using different stages provided for the top view and cross-sectional view of the sample.

One downside of the SEM process is that samples must be cut down before loading them in the microscope. This sometimes might damage the sample and cracks are visible while imaging. The other method that can be used to measure thickness is ellipsometry but nc-si:H on textured Al foil cannot be measured in this process. Also, measuring the cross-section can be tedious sometimes as the thick Al layer after cutting over-shadows the TCO layer.

For this thesis work various samples of bare aluminium foils, untreated and pre-treated Al foil, Al + TCO, and TCO + Carrier foils are used. Both top and cross-section imaging is performed to check various features. While using the Al-based samples the acceleration voltage is maintained at 10 Kv and if the sample is reflective then auto contrast mode is used. For PEN-based samples, the acceleration voltage is brought down to 1 Kv as the sample might melt at a higher voltage.

3.2. 3D Laser Scanning Microscope :

The Keyence VK-X250 3D Laser Scanning Confocal Microscope provides data on nanometer-level profile, roughness, and film thickness of any material without contact [32]. It is fast and easy to use compared to SEM but doesn't provide as accurate compared to SEM. This microscope has a lateral resolution of 120 nm by using a violet laser light of 408 nm and 0.5 nm of depth resolution [32].

The microscope uses a 16-bit photomultiplier to receive the reflected laser light and scan the surface. Also, it can provide 3D measurement data over any shape of the material and steep angle (up to 88^{o} angle of detection) accurately. Four lenses available in this microscope are 10x, 20x, 50x, and 150x respectively [32].

Figure 3. 2: 3D Laser scanning microscope by Keyence [33].

To detect the height information of the sample laser microscope uses the confocal principle. An optical system in which a pinhole is incorporated before the light-receiving element is called a confocal optical system and this type of detection principle is called the confocal principle. Point light source is used for an optical scanner to capture the surface shape using laser light in the X and Y direction. Thus, the reflected light windows divided into pixels are

detected by the light-receiving element. A motor is used to move the objective lens and the position of the objective lens, and the amount of light received by the light-receiving element is detected. Finally, we can detect the focus position of the sample by changes in the amount of received light [32].

For this thesis work measurements on a 3D Laser, Microscope was done extensively. To maintain uniformity in the readings and purpose of calculations x20 and x50 lenses were used for measuring various surface roughness parameters. Like SEM in this microscope as well we have to cut the samples. The sample is then placed uniformly in the sample holder using double-sided tape so that it doesn't damage the lens.

3.3. Spectrophotometer :

To measure the surface texturing of the sample optical characterization is an important parameter. For this study, we are using a PerkinElmer® Lambda 1050 spectrophotometer with an Integrating Sphere (IS). The spectrophotometer uses two lamps namely: deuterium arc lamp and tungsten-halogen lamp that covers the wavelength range between 175 nm – 3300 nm [34]. The monochromatic light source is at an angle of 5° with the sample so that the incident ray and reflected light do not interfere [35]. The reflected light we get finally has two parts diffuse and specular. A slit port next to the monochromatic light source is removed while measuring the diffuse part of the light.

Figure 3. 3: PerkinElmer® Lambda 1050 spectrophotometer with Integrating sphere setup [34].

Depending on the type of measurement the sample is placed in different locations. While measuring the reflectance, the sample is placed at the end of the spectrophotometer and for transmittance, the sample is placed inside the spectrophotometer. The user can specify the range of wavelength and the resolution but generally, it is kept between 1200 nm to 300 nm, and a resolution of 5 nm.

3.4. Hall Effect Measurement :

Various electrical properties of the thin film that is deposited like electron mobility, resistivity, bulk concentration, and sheet concentration can be calculated using the hall effect setup. Hall effect measurement is based on the Lorentz force and Van der Pauw method.

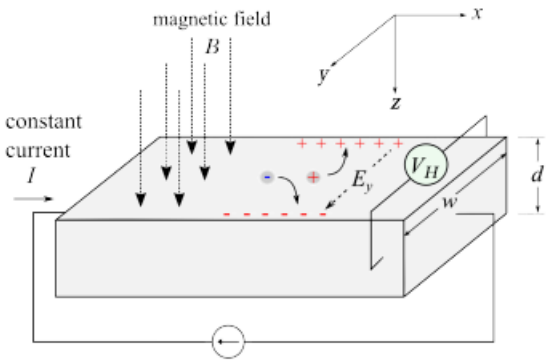

Figure 3. 4: Hall effect illustration [36]

$$(FL) = q \cdot v \times B \qquad (3.1)$$

Where, q = charge carriers ;
v = velocity ;
B = magnetic field.

During the measurement, a sample is placed on a board which four-point probes are connected at the corners as shown in figure 3.5 to which a perpendicular magnetic force is applied. A magnetic force is experienced by the electrons when current flows through the sample and move towards the sample side. The resulting difference in charge causes the voltage drop across the sample called Hall voltage. The sample sizes are generally taken as 10 mm x 10 mm for best results [37].

(a) (b)

Figure 3. 5: Hall effect setup: (a) Sample mount (b) Sample stage [37]

3.5. Atomic Force Microscopy (AFM) :

An AFM is a microscope with a cantilever arm that has a sharp tip on its end which is used to scan the specimen surface as shown in figure 3.6. The tip sweeps across the surface because of which the force between the atom from which the tip is made and the atoms on the surface changes constantly causing the cantilever to bend. This bend in the cantilever is detected by bouncing a laser beam off its surface. The distance the laser beam travels can be used to measure the amount the cantilever bends and the forces acting on it. Finally, this data can be used to measure and plot the contour of the surface [31].

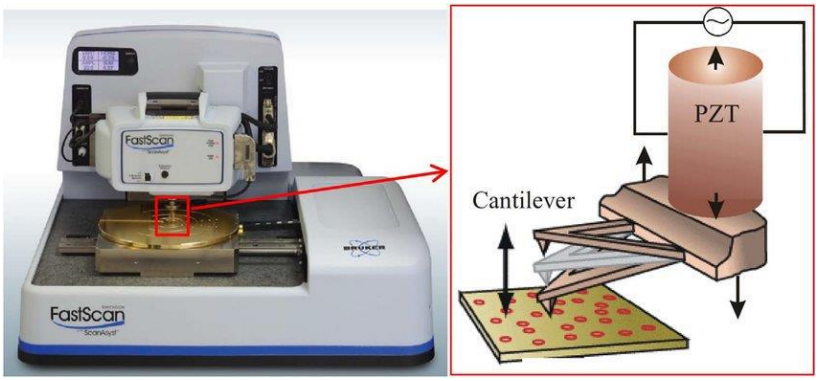

Figure 3. 6: Atomic force microscope setup

Various parameters that can be calculated from the resulting AFM images are the correlation length (L_c), root mean square (RMS) roughness (σ_{rms}), and the aspect ratio. The σ_{rms} values give an idea of the roughness of the sample, a higher σ_{rms} value indicates more sharp features on the surface. The values are calculated using the equation:

$$\sigma_{rms} = \sqrt{\frac{1}{N}\sum_{i=1}^{N}(Z_i - \bar{z})^2}$$

Where, N = number of data points;

Z_i = height at the ith position;

$\bar{z}$ = average surface level.

The other parameter correlation length (L_c) is used to find the horizontal roughness of the sample and gives the diameter of micro-sized craters [17]. The software used for characterizing is Nanoscape Analysis 2.0 and Gwyddion. The AFM measured sample is flattened through Nanoscope and by using Gwyddion the RMS roughness and correlation length are calculated. Finally, the aspect ratio is calculated by taking the ratio between σ_{rms} and L_c ($\frac{\sigma_{RMS}}{L_c}$).

4

Results and discussion

4.1. Bare Aluminium foil:

4.1.1. Structural Characterization using 3D Confocal Microscope:

This is a round-robin 3D measurement on bare aluminium foils to find out which measurement technique can be used to characterize the foils. The method used here is a 3D confocal microscope and this correlates with one of the companies. This will help HyET solar to do quality analysis on its foil after receiving them from the supplier.

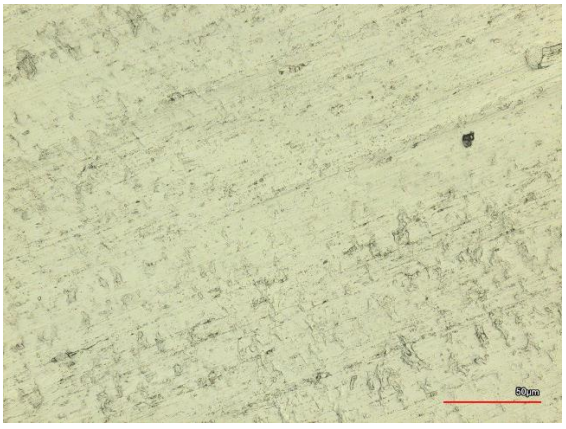

(a)

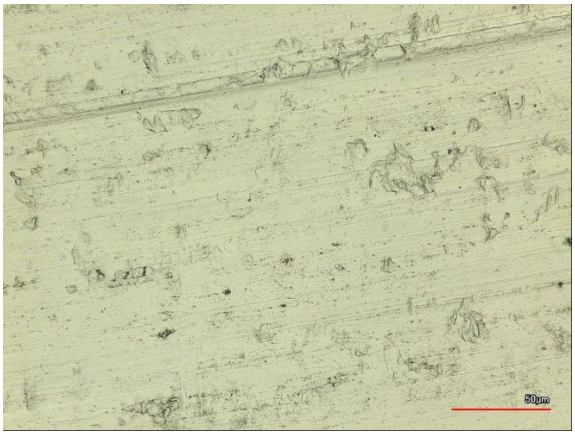

(b)

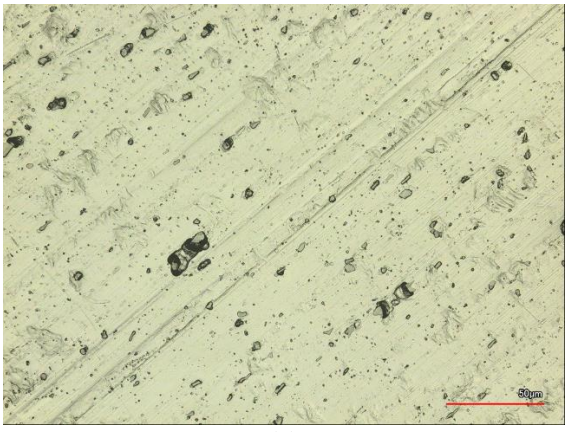

(c)

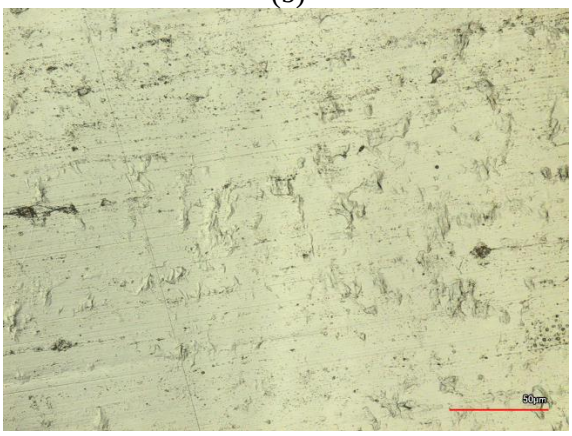

(d)

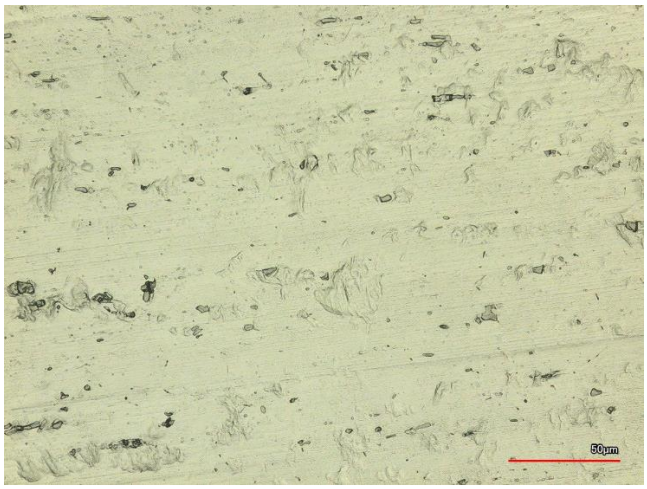

(e)

Figure 4. 1: 3D confocal images of bare aluminium foil samples which are: (a) 2011-Un-treated (b) 2020-Un-treated (c) Pre-treated (d) Annealed (e) Annealed + pre-treated

In figure 4.1 above we see the 3D confocal microscope images from the five samples and each having three sets. For each of the samples, three different areas were measured for different roughness parameters. Milling tracks are visible in all the samples except the annealed and annealed + pre-treated. Also, in the pre-treated samples, we can see the presence of precipitants.

Now the roughness parameter comparison was done between the five samples for Surface max peak-to-pit height (Sz) and Surface summit curvature (Spc). Surface max peak-to-pit height gives us the sum of the largest peak height value and the largest pit depth value within the selected area. Axis surface summit curvature gives the arithmetic mean of the principal curvature of the peaks that is present on the surface [38].

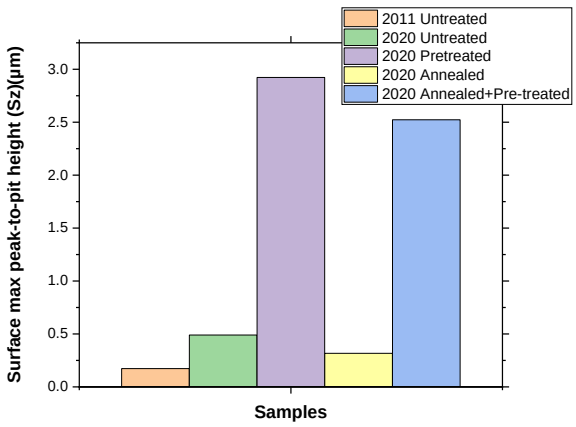

Figure 4. 2: Surface max peak-to-pit height between bare aluminium foil samples.

In figure 4.2 we can see that the major peak is in the 2020 pre-treated sample which is mainly due to pinholes and milling tracks. Pre-treating the foil introduces precipitants as well which confirms the increase in Sz value from 2020 untreated to pre-treated and 2020 annealed to 2020

annealed + pre-treated. After pre-treating the samples, the surface gets rough and sharp as we are creating craters.

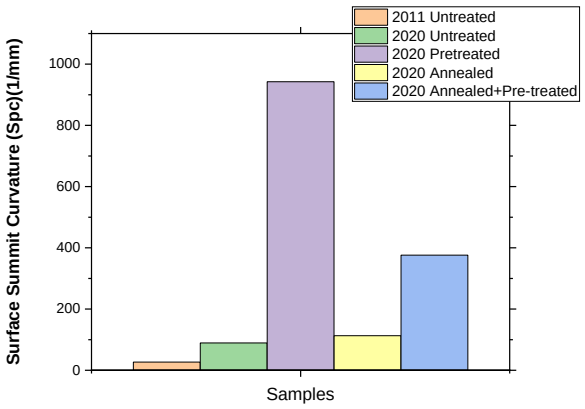

Figure 4. 3: Surface summit curvature between bare aluminium foil samples

Surface summit curvature tells the shape of the peaks in which a smaller value indicates that there are rounded shapes at the point of contact with other objects and a larger value indicated there are pointed shapes at the point of contact with objects. A higher peak in the 2020 pre-treated sample in figure 4.3 would be due to the presence of milling tracks and pinholes. We can see from the graphs above that due to annealing of the aluminium foil there is less surface roughness, a decrease in milling track roughness, and a reduction in pinhole density. But annealing before texturing does not have much impact on the surface parameters [23].

Here in figures 4.4 and 4.5, we see the surface max peak-to-pit correlation and surface summit curvature correlation between the values of the two companies and the values taken at TU Delft. When it comes to roughness analysis it's a difficult method because depending on where we are measuring, we might end up getting a different texture eventually leading to different results. Because in round-robin experiment as well the companies measure the foils and HyET sends the sample to TU Delft from the foil. So, the main idea would be having similar morphological values that correlate with the values of the company. The two companies were using different methods like white light interferometry and confocal microscopy. These methods were used by HyET considering the cost and availability. This is supposed to be used as a quality control method and around 100 samples are to be measured every year so to do it cost-effectively. The reading was taken at Delft through a confocal microscope correlated with a company that uses the same method.

Possible to measure the same foil even if samples are taken at different lengths of foil to measure and correlate the values. By this HyET solar can do their quality control and check that the supplier is providing them with the required quality foil.

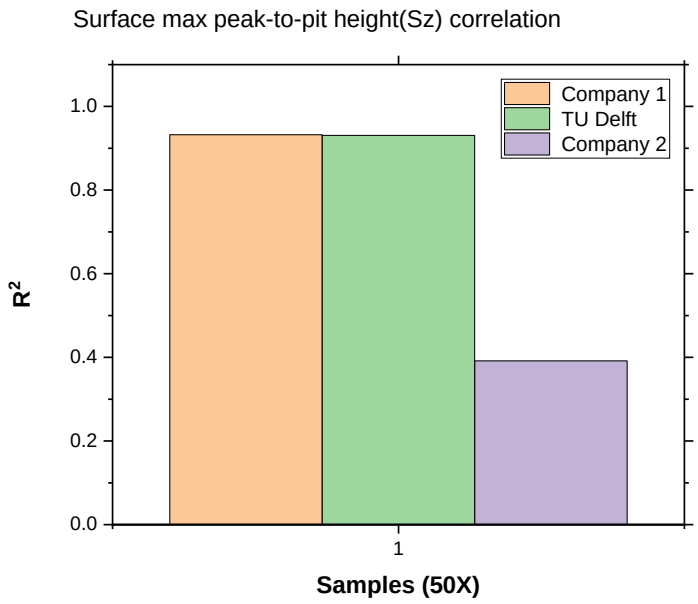

Figure 4. 4: Surface max peak-to-pit height correlation for bare aluminium foil samples

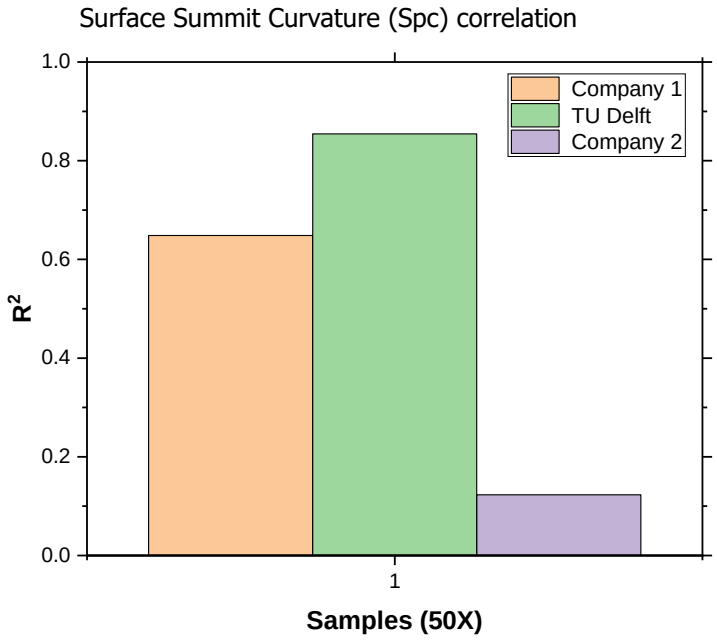

Figure 4. 5: Surface summit curvature correlation for bare aluminium foil samples

4.2. Baseline Textured Sample:

4.2.1. Structural Characterization using 3D Confocal Microscope:

In this characterization series, a total of 24 samples were used which included 2020 untreated and baseline samples, 2021 untreated and baseline samples, and FLAM02 textured samples. Below Figures 4.6 and 4.7show the structural image of both 2020 and 2021 baseline pre-treated aluminium foils. The resolution used was 50x to have a close-up view of the sample.

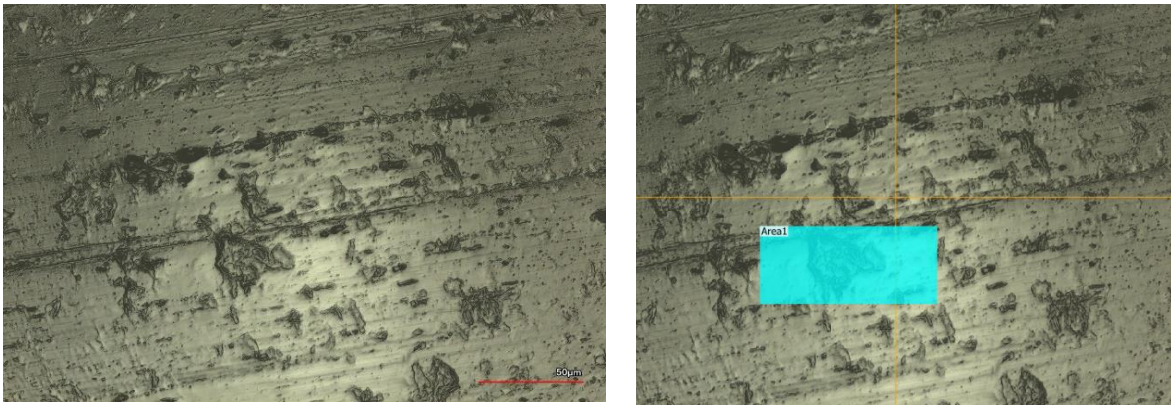

(a) (b)

Figure 4. 6: 3D confocal images of 2020 pre-treated aluminium foil: (a) Pre-treated (b) Area to be characterized

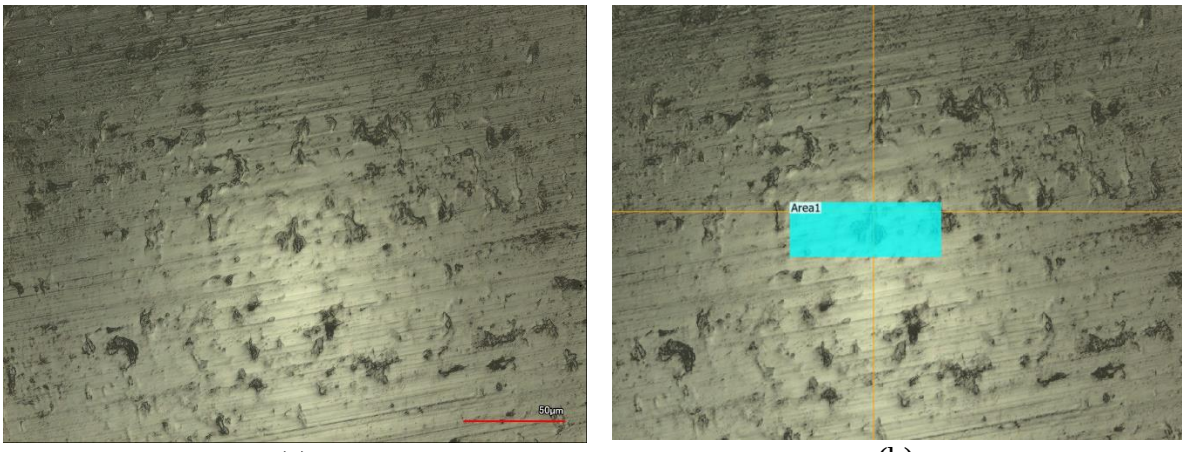

(a) (b)

Figure 4. 7: 3D confocal images of 2021 pre-treated aluminium foil: (a) Pre-treated (b) Area to be characterized

Comparing both the 2020 baseline and 2021 baseline sample we can see that the 2020 baseline sample has milling tracks and more rough morphology as compared to the 2021 sample.

Figure 4.8, 4.9, and 4.10 below give a comparison between various roughness parameters like Arithmetic mean height (Sa), Surface max peak-to-pit height (Sz), and Axis surface summit curvature (Spc) between untreated 2020 samples, untreated 2021 samples, factory baseline 2020 and factory baseline 2021.

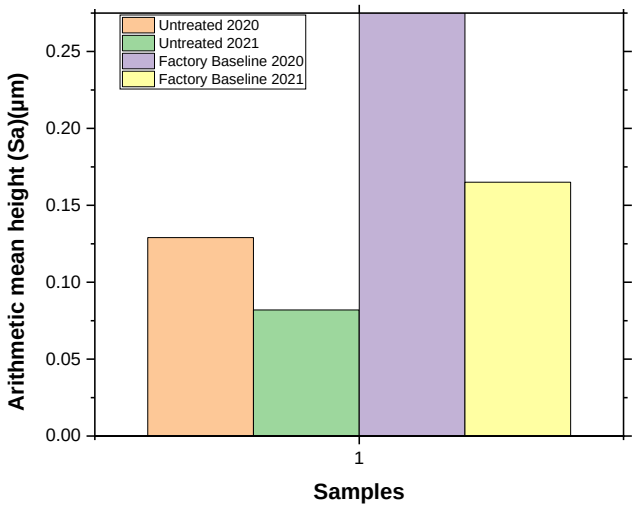

Figure 4. 8: Arithmetic mean height between untreated 2020, untreated 2021, factory baseline 2020, and factory baseline 2021

Arithmetic means height gives the height difference of each point when compared to the arithmetic mean of the surface. Generally, we use this parameter to measure the roughness of a surface [38]. As seen in figure 4.8 the 2021 untreated foil has lower roughness as compared to 2020 untreated foil. Factory baseline 2021 has less roughness that could be lesser milling tracks and pinholes as compared to factory baseline 2020.

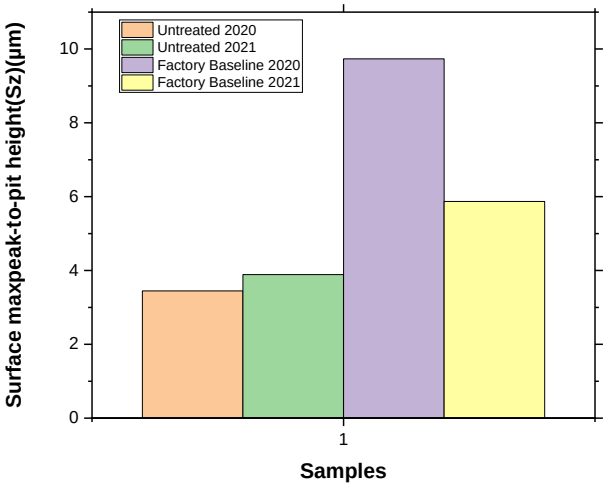

Figure 4. 9: Surface max peak-to-pit height between untreated 2020, untreated 2021, factory baseline 2020, and factory baseline 2021.

In figure 4.9 the untreated 2020 and 2021 foil has very little change in height. For the factory baseline foils, we see that there is an improvement in the 2021 baseline foil. The higher value of the 2020 factory baseline foil could be due to more milling tracks and pinholes.

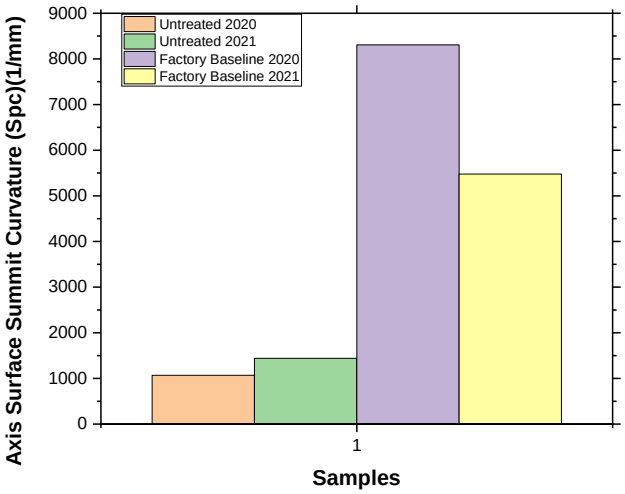

Figure 4. 10: Axis surface summit curvature between untreated 2020, untreated 2021, factory baseline 2020, and factory baseline 2021

For axis surface summit curvature in figure 4.10, we can see a higher value in the factory baseline 2020 sample due to the presence of sharper features that gives a higher value. But we can see improvement in the factory baseline 2021.

4.2.2. Structural Characterization using SEM:

In SEM imaging different portions of the same foil are used, and the milling tracks are analyzed. The images were taken at various resolutions of 50 µm, 30 µm, 10 µm, and 5 µm. In figure 4.11 (b) the thickness of the milling track is shown to be around 9.047 µm. From both the images in figures 4.11 and 4.12 we can see the presence of precipitants scattered through samples. But compared to 2020 we see a reduction in precipitants in 2021.

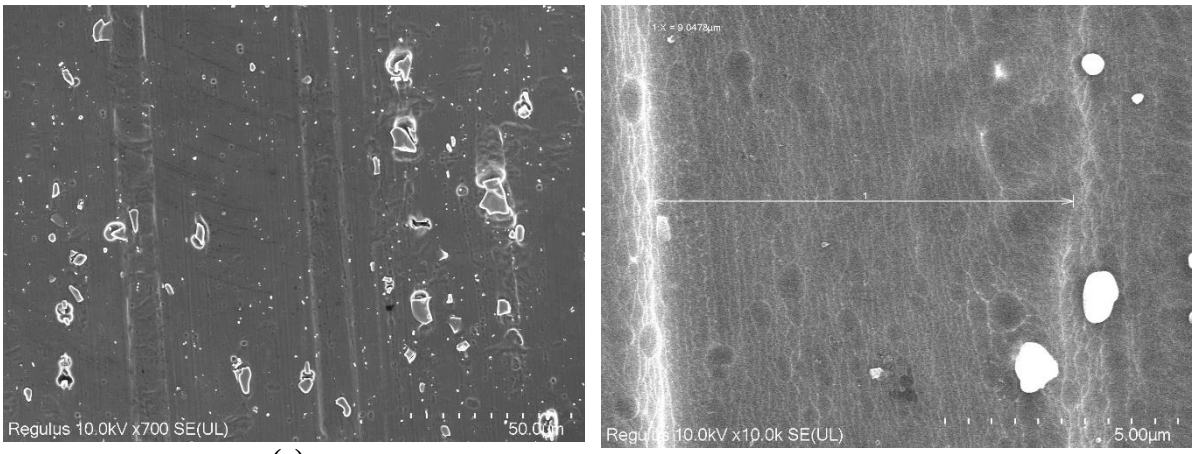

(a) (b)

Figure 4. 11: SEM imaging of factory baseline 2020 at: (a) 50 µm (b) 5 µm

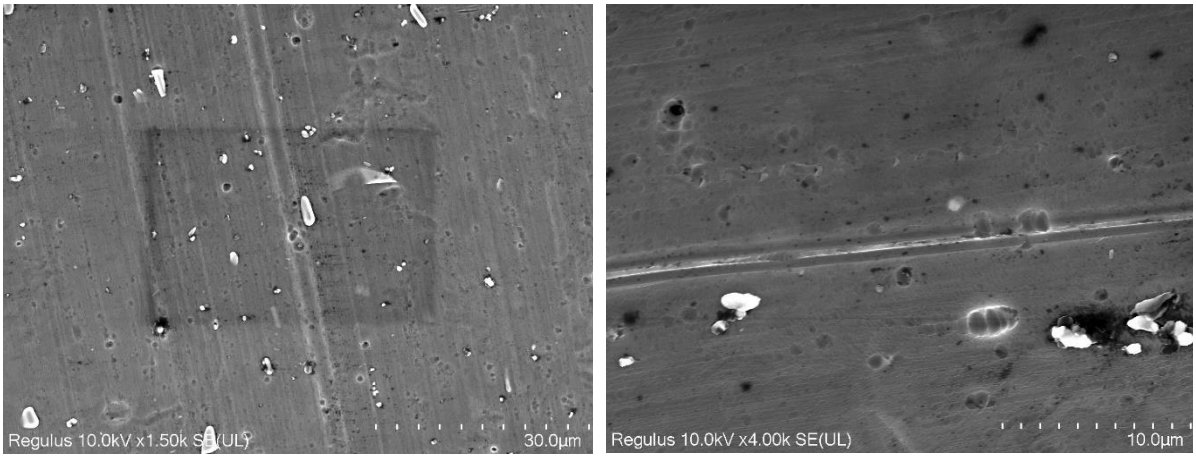

(a) (b)

Figure 4. 12: SEM imaging of factory baseline 2021 foil at: (a) 30 µm (b) 10 µm

Milling tracks are bad for the solar cells as they increase the roughness of the foil. Thus, this gets carried to the further layers of the solar cell and can finally lead to a deformed solar panel. Maximum number of samples here showed milling tracks and pinholes in them, and they might have been transferred from the bare foil as even after texturing we don't see much reduction in the milling tracks.

4.2.3. Optical Characterization using Spectrophotometer:

Here in figure 4.13, we see the diffuse and specular reflectance of the factory baseline sample that is textured for the years 2020 and 2021. The light after reflection can be divided into two types: diffused and specular reflection. The light which is reflected from a smooth surface at a definite angle is called specular reflection and light that is reflected from a rough surface at several angles is called diffused reflection.

The reflectance value is 0.35 in the visible wavelengths for both 2020 and 2021 factory baseline samples. For the specular part of the reflection, we see a small increase in the value in the 2020 sample compared to the 2021 sample more towards the UV region. For the visible region, the reflectance varies between 0.57 for the 2020 factory baseline and 0.55 for the 2021 factory baseline. From this point of view, the foils have very similar properties.

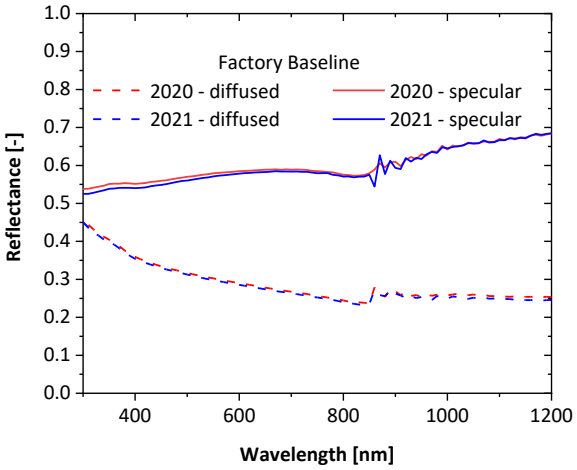

Figure 4. 13: Reflectance for factory baseline foil

4.3. FLAM02:

4.3.1. Structural Characterization using a 3D confocal microscope:

The FLAM02 process is based on a 150 μm thick aluminum foil. Figure 4.14 below shows the FLAM02 textured foils that are characterized in the confocal microscope. We can see the craters more clearly and the reduction in milling tracks.

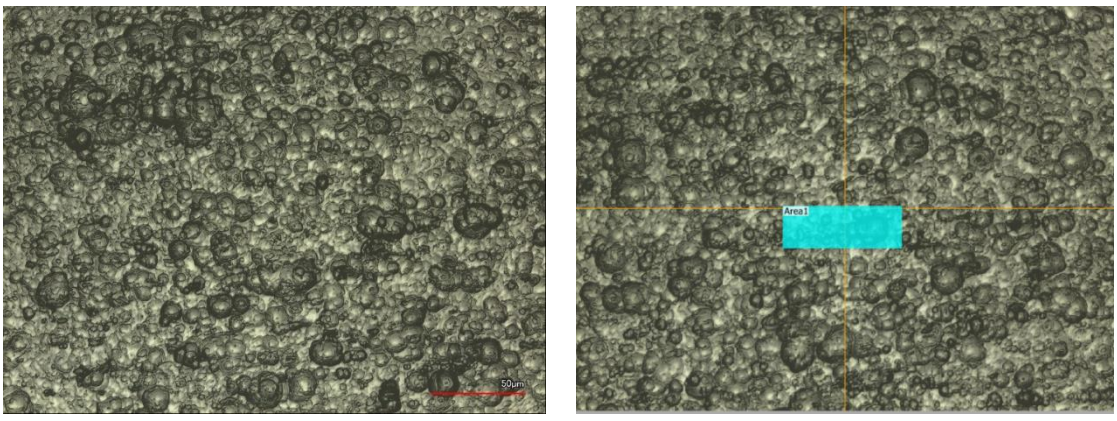

(a) (b)

Figure 4. 14: 3D confocal images of FLAM02 textured foils showing: (a) FLAM02 textures (b) Area that is characterized

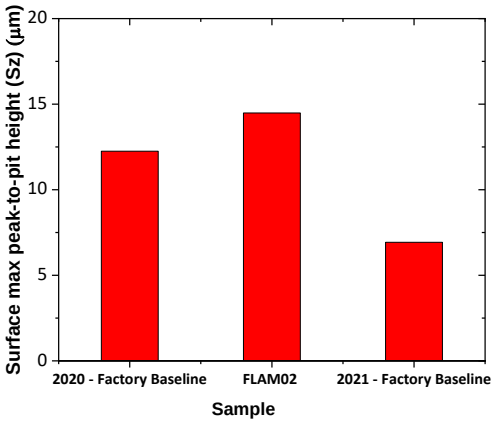

Figure 4. 15: Surface max peak-to-pit height between factory baseline 2020, factory baseline 2021, and FLAM02 texture

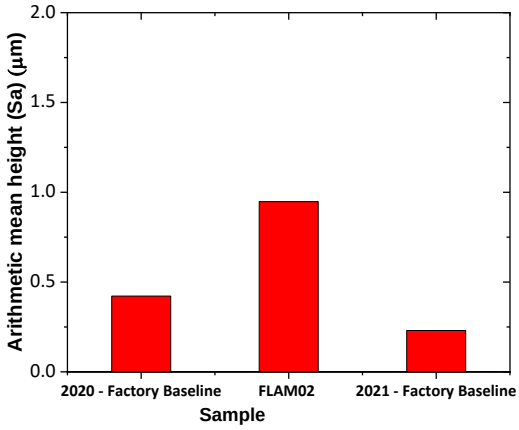

Figure 4. 16: Arithmetic mean height between factory baseline 2020, factory baseline 2021, and FLAM02 texture

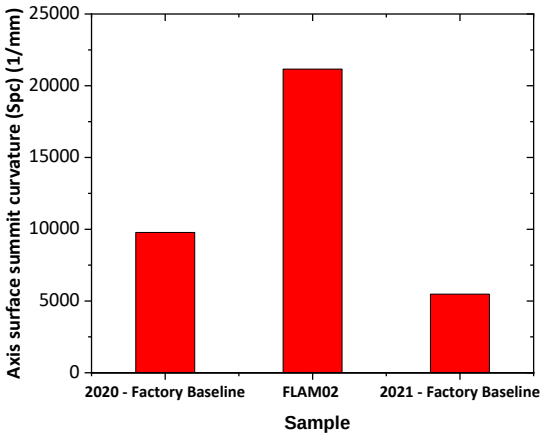

Figure 4. 17: Axis surface summit curvature between factory baseline 2020, factory baseline 2021, and FLAM02 texture

Figures 4.15, 4.16, and 4.17 above show various roughness parameters like Surface max peak-to-pit height (Sz), Arithmetic mean height (Sa), and Axis surface summit curvature (Spc) between 2020-factory baseline, FLAM02, and 2021-factory baseline. The increase in roughness values is notable in FLAM02 for all parameters and this seems to have a positive impact on the optical parameters of the foil, like higher diffuse reflectance and haze.

As we can see here in FLAM02 the roughness is increased in this texturing. There is increased photo-response and increased adhesion. Texturing is so strong that imperfections like milling tracks are eliminated. Till now no devices have been made in FLAM02 and FLAM01 textured foils as during attempts in FLAM01 textured foils all of them shunted. Also, the presence of precipitants makes it difficult for TCO deposition.

4.3.2. Structural Characterization using SEM:

Here the SEM imaging of the FLAM02 texturing done on the aluminium foil is done. To have a close and clear view of the texturing resolution of 20 μm and 10 μm is used which can be seen in figure 4.18 below. Compared to the baseline texturing that was shown in the images above the texturing in FLM02 is more uniform and we see no milling tracks and fewer pinholes as in FLAM02 texturing there is a good amount of aluminium etched away. The uniform texturing done here helps in a proper deposition in further steps. Also, this causes fewer problems due to cracks as the roughness is significantly less in the FLAM02 texturing.

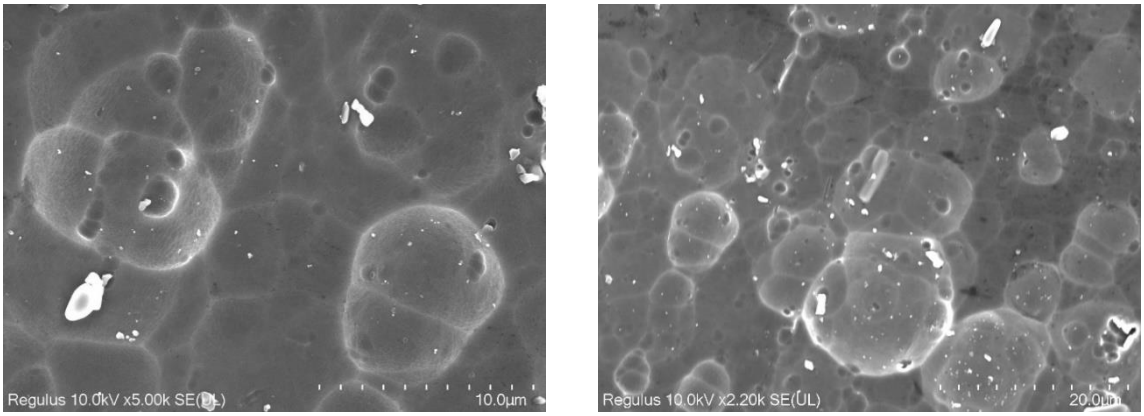

(a) (b)

Figure 4. 18: SEM image of aluminium foil with FLAM 02 texturing at: (a) 10 μm (b) 20 μm

One primary issue that still resides in this sample is the presence of precipitants. As we can see in figure 4.19 below there is still a good amount of precipitants present in the sample. Precipitants are introduced in the sample after the pre-treatment process of the aluminium foil primarily for the removal of oil from the surface of the foil to texture it and then the texturing of the foil. This is mainly because the impure aluminium is used as pure aluminium would melt.

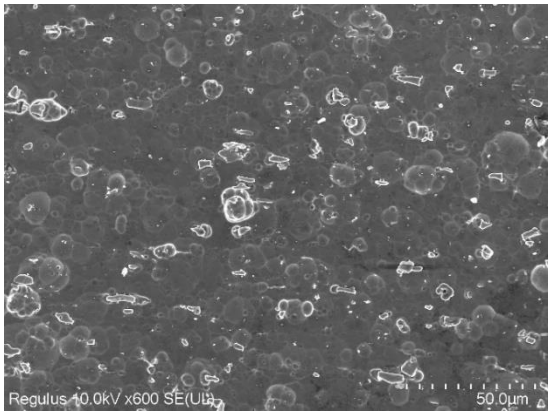

Figure 4. 19: Presence of precipitants in the sample

4.3.3. Structural Characterization using AFM:

Figure 4.20 and 4.21 below shows the 2D and 3D images of the FLAM02 texturing taken using AFM. For characterizing the structural properties further and calculating the RMS roughness, autocorrelation length, and the aspect ratio of the features AFM imaging is done.

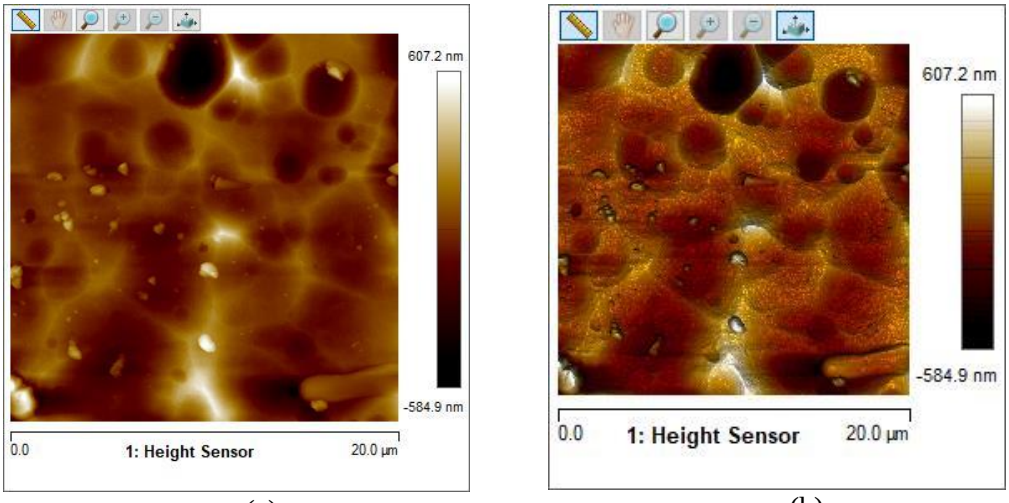

(a) (b)

Figure 4. 20: 2D AFM imaging of FLAM02 texturing

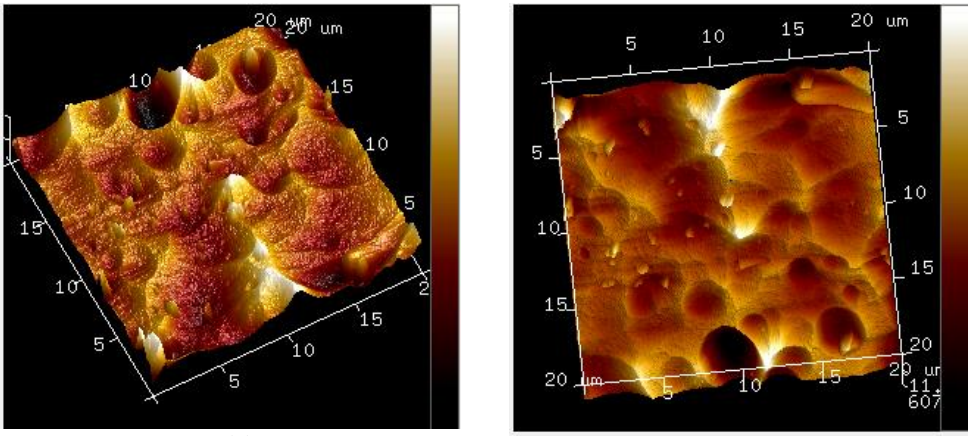

(a) (b)

Figure 4. 21: 3D AFM imaging of FLAM02 texturing

In the 3D imaging of the sample, we can see the craters of the FLAM02 texturing more properly when the image is moved to an angle. On the top side, we can see the smooth features and at the bottom, we can see the craters.

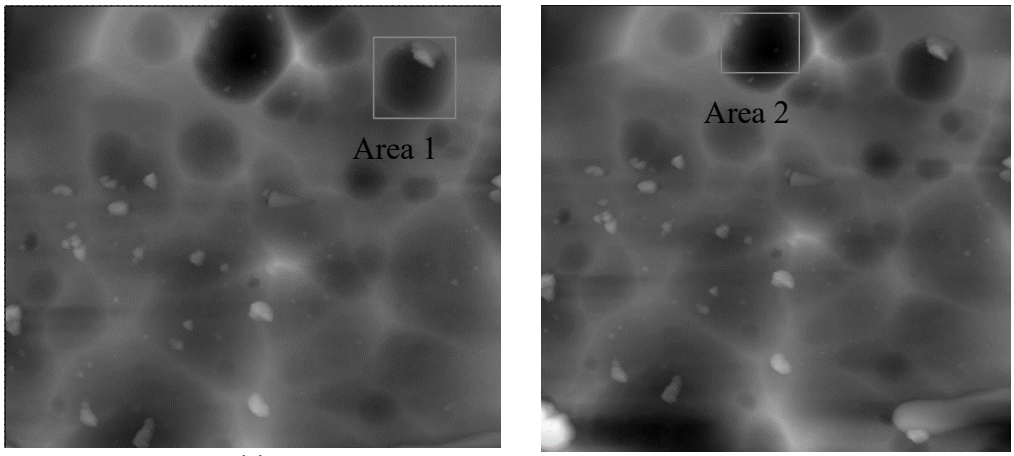

(a) (b)

Figure 4. 22: Gwyddion images showing the areas used for calculating structural parameters

By using the Nanoscope analysis software the AFM images are flattened to remove unwanted features like noise and tilt. Then the image is opened in Gwyddion software to calculate the RMS roughness (σ_{rms}), autocorrelation length (L_{c}), and the aspect ratio (σ_{rms}/ L_c).

Area	RMS roughness (σ_{rms}) (nm)	Autocorrelation length (L_c) (μm)	Aspect ratio (σ_{rms}/L_c)
Whole	161.3	1.36	0.118
1	163.5	1.69	0.096
2	260.1	2.17	0.119

Table 4. 1: Surface morphology characterization parameter values

The RMS roughness represents the depth of the craters whereas the autocorrelation length gives us the width of the craters. Here the total area of the sample and two areas are taken as shown in figure 4.22. Then from these aspect ratios is calculated which is the ratio of σ_{rms} and L_c. A good aspect ratio of a crater is usually 12% for good quality nc:si. In our calculation we find that the aspect ratio of the whole area is 11.8%, for area 1 is 9.6% and for area 2 is 11.9%.

4.3.4. Optical Characterization using Spectrophotometer:

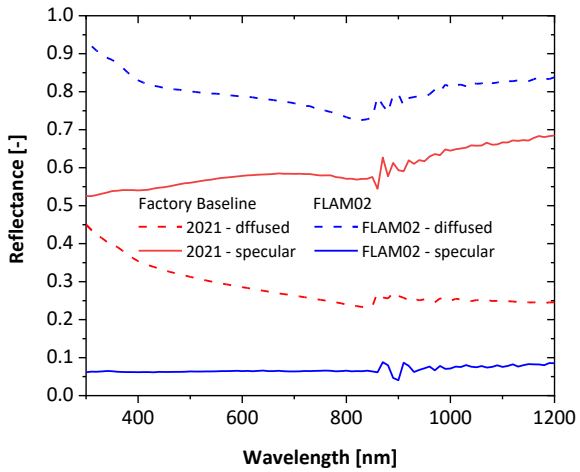

Figure 4. 23: Reflectance comparison between factory baseline and FLAM02 texturing

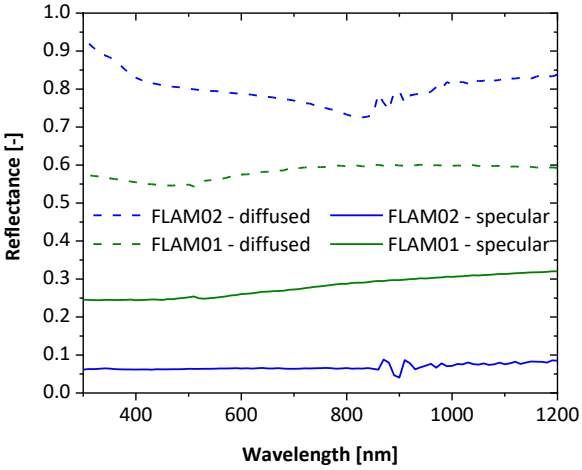

Figure 4. 24: Reflectance comparison between FLAM01 and FLAM02 texturing

In figure 4.23 above we can see the reflectance comparison between factory baseline texturing for 2021 and FLAM02 texturing for 2021. In figure 4.24 we can see the comparison between the FLAM01 and FLAM02 texturing for both diffused and specular reflectance. Both compared to FLAM01, and factory baseline the diffused reflectance has a higher value. Therefore, we can say that FLAM02 scatters light much better than the previous two substrates.

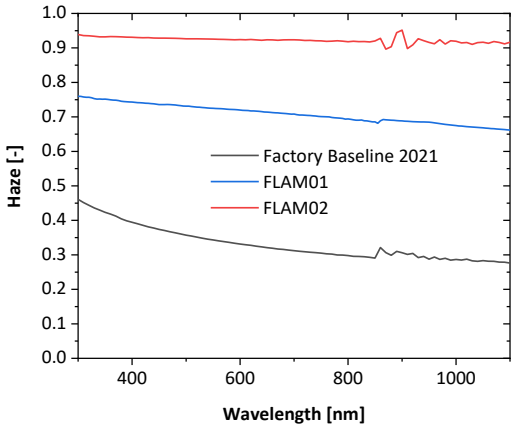

Figure 4. 25: Haze value for different texturing

In figure 4.25 the haze between different texturing's is compared. We can see from the graph that FLAM02 has the highest haze value which corresponds to a higher diffused reflectance, and this means a higher scattering of the light.

4.4. Al + TCO based samples:

4.4.1. Structural Characterization using 3D Confocal Microscope:

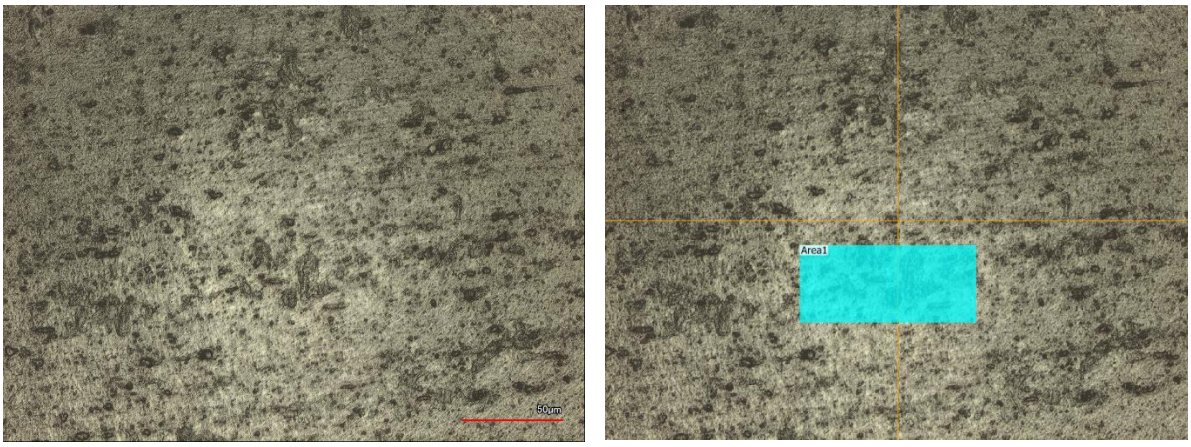

(a) (b)

Figure 4. 26: 3D Confocal images of: (a) Al + TCO pre-treated sample (b) Area that is characterized

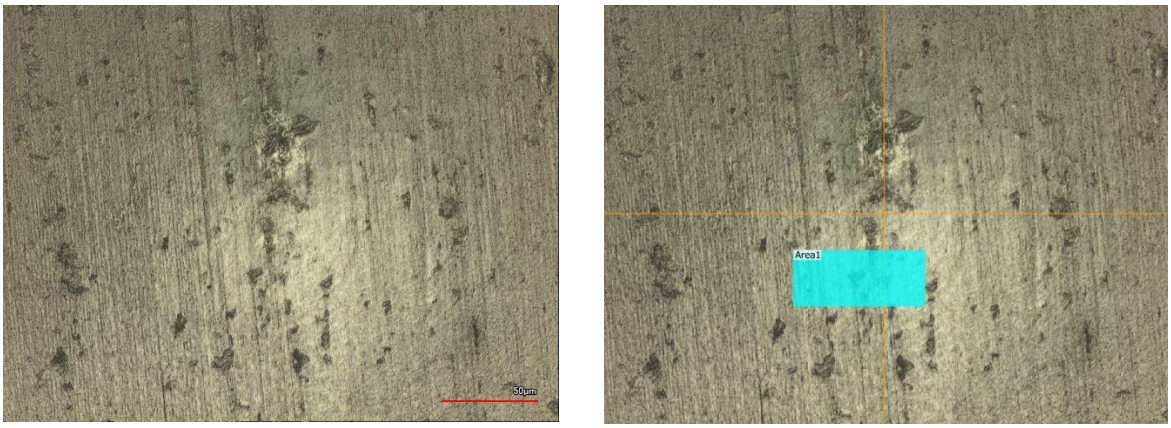

(a) (b)

Figure 4. 27: 3D Confocal images of: a) Al + TCO untreated sample (b) Area that is characterized

Figure 4.26 and 4.27 above shows the 3D confocal images of Al + TCO pre-treated and untreated samples. Image (b) shows the area that is characterized, and the roughness parameters are explained further in the graphs below.

The graphs below in Figures 4.28, 4.29, and 4.30 show various roughness parameters comparison between Al + TCO pre-treated and untreated samples of different TCO thicknesses. Overall, we can see that the Al + TCO pre-treated sample has a higher value compared to Al + TCO untreated samples due to precipitants that get added to the pre-treated foils. Milling tracks and pinholes present in the bare foils are transferred to the TCO as well

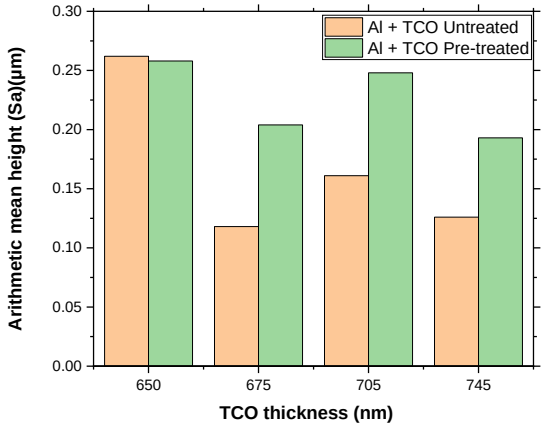

Figure 4. 28: Arithmetic mean height between Al + TCO untreated and Al + TCO Pre-treated

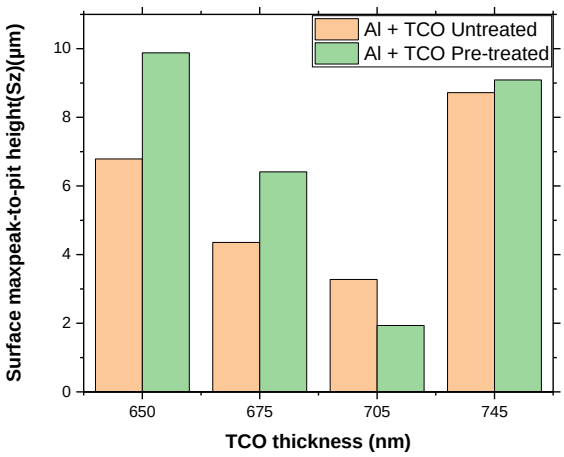

Figure 4. 29: Surface max peak-to-pit height between Al + TCO untreated and Al + TCO Pre-treated

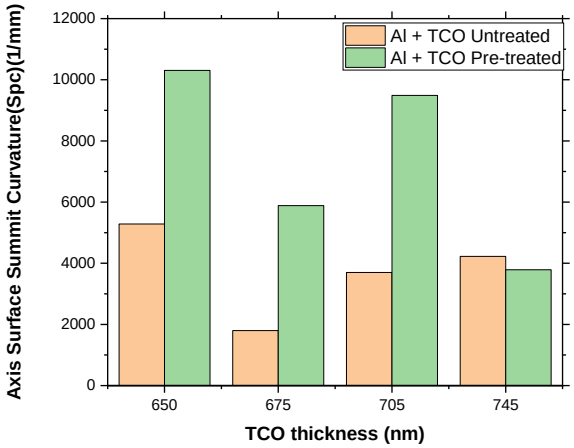

Figure 4. 30: Axis surface summit curvature between Al + TCO untreated and Al + TCO Pre-treated

4.4.2. Structural Characterization using SEM:

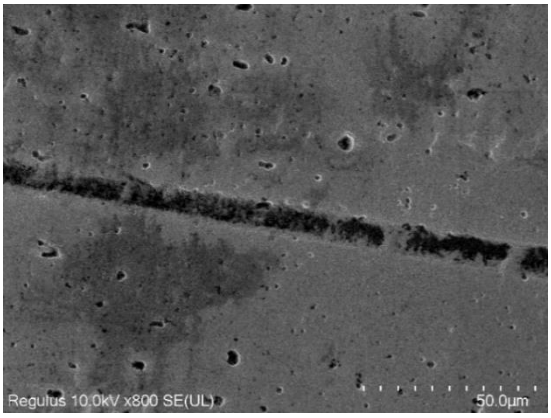

(a)

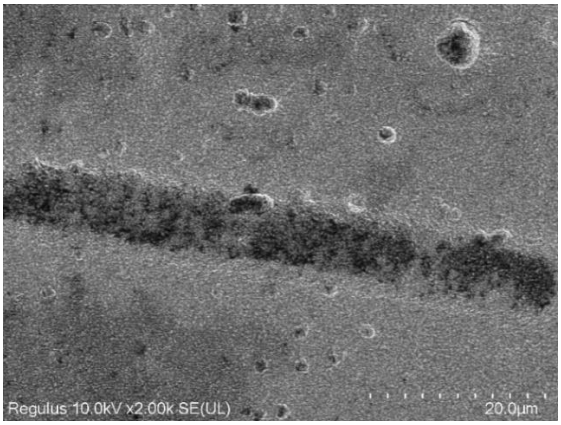

(b)

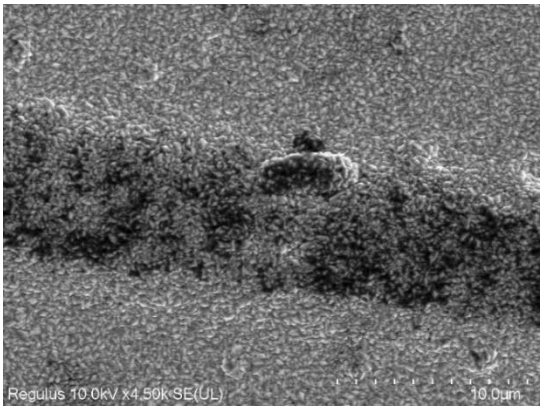

(c)

Figure 4. 31: SEM image of baseline pre-treated TCO + Al sample at: (a) 50 µm (b) 20 µm (c) 10 µm

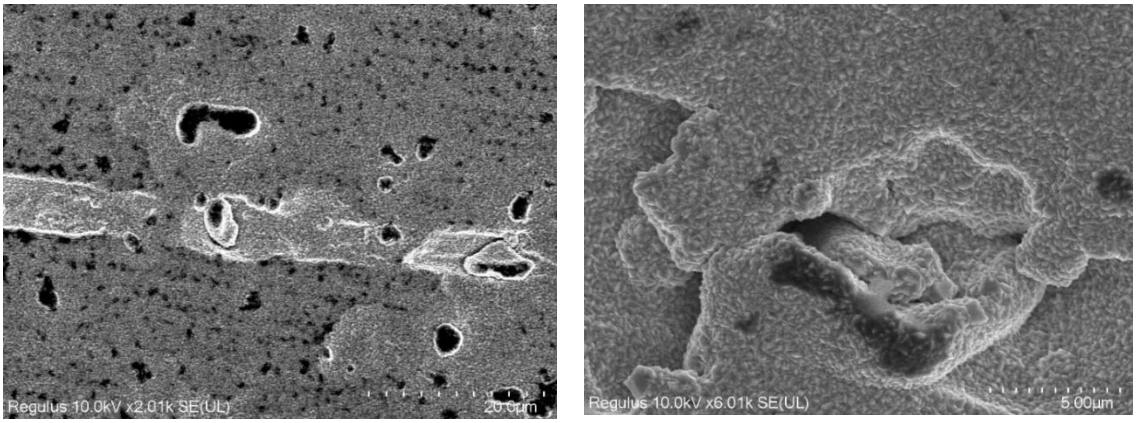

(a) (b)

Figure 4. 32: SEM image of pre-treated TCO + Al sample with varying TCO thickness at: (a) 20 µm (b) 5 µm

Both the baseline and pre-treated samples belong to the pre-treated series. From figure 4.31 (a), (b), and (c) above we can see the milling tracks at a resolution of 50 µm, 20 µm, and 10 µm of SEM. In figure (a) at 50 µm the milling track is visible which passes like a straight line. For figures (b) and (c) as we zoom in further, we can see the crystal structure of the TCO and the milling tracks on a better scale. These tracks have been introduced when the aluminium foils are processed before HyET receives them. For the pre-treated aluminium foils deposited with TCO shown in figure 4.32, we can see the milling tracks as well as cracks in the TCO. This shows that if the foil has milling tracks and cracks that are introduced in the TCO layer as well when it is deposited. Also, we can see the presence of precipitants in both foils.

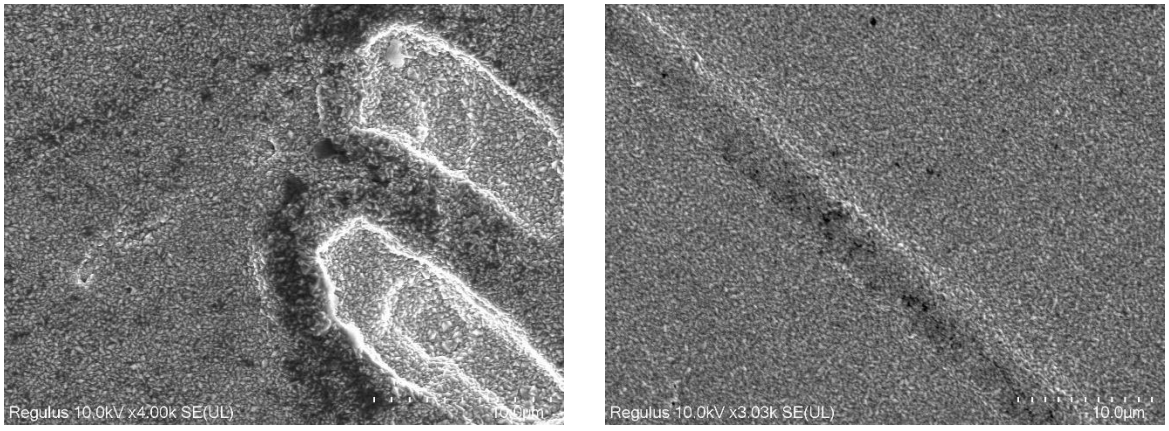

(a) (b)

Figure 4. 33: SEM image of un-treated TCO + Al sample (a) 10 µm (b) 10 µm

Now we see the SEM imaging of the un-treated aluminium foil in figure 4.33. The major difference from the pre-treated samples is the absence of precipitants but we still find milling in the foil. Also, we see the island of TCO in figure (a) due to the roughness of foil that causes uneven deposition of TCO in the foil. The islands could also be due to this could be due to

particle contamination during APCVD(particles forming in the gas phase before getting deposited on the Al).

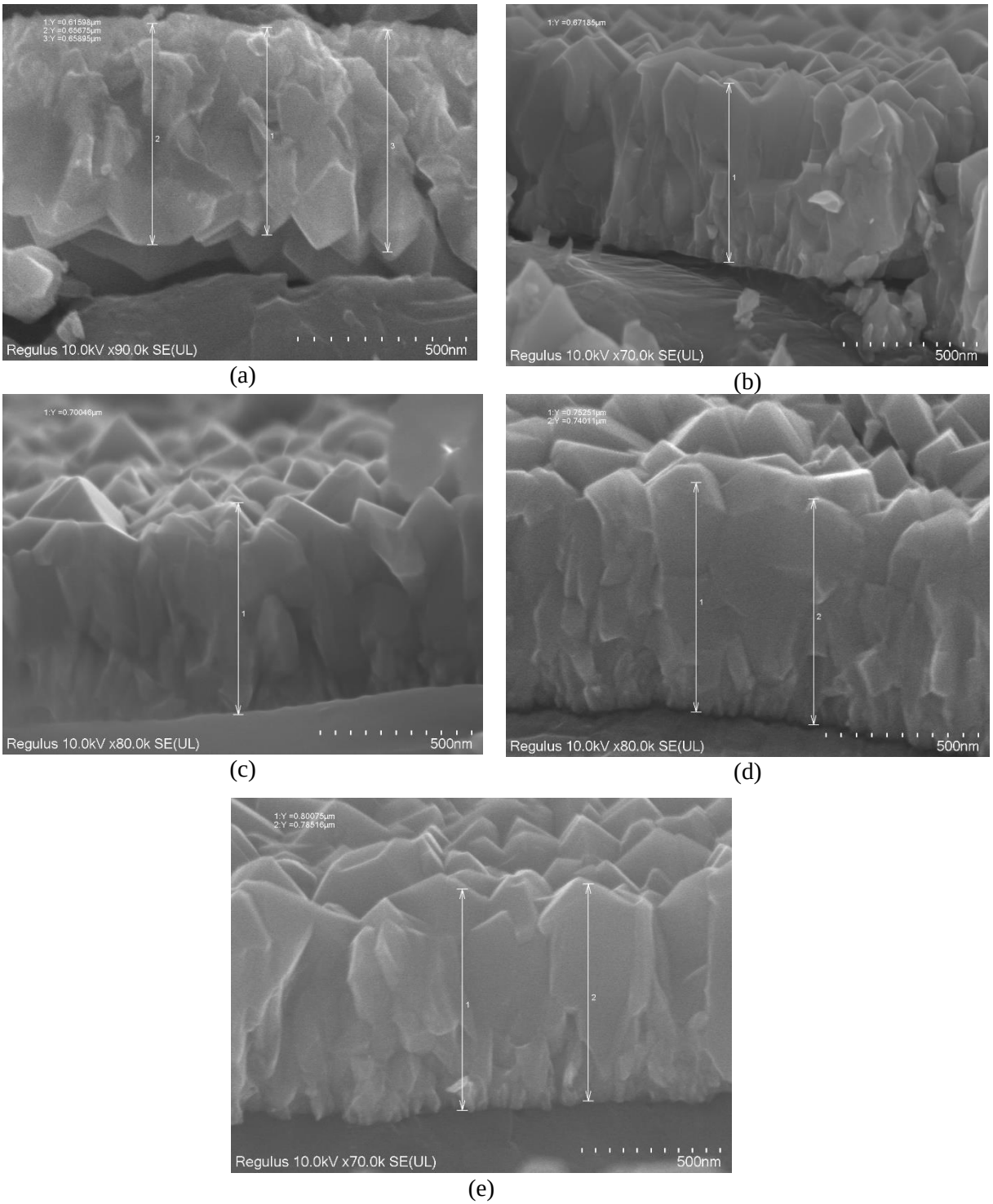

Figure 4. 34: Front view of TCO with different thickness of: (a) 656.7 nm (b) 671.8 nm (c) 700.46 nm (d) 740.11 nm (e) 785.16 nm

In figure 4.34 we have different thicknesses of TCO deposited on the aluminium foil. The respective thicknesses are 650 nm, 675 nm, 705 nm, 745 nm, and 790 nm and from the images above we can see that the deposited layer is almost similar. By this, we can confirm the

thickness of the sample using the optical thickness method and the order of magnitude is pretty similar.

4.4.3. Optical Characterization using Spectrophotometer:

The graphs below are shown in figures 4.35 – 4.39 the relation between reflectance and wavelength for different TCO thicknesses for AL + TCO samples. For the short wavelength region between 400 nm to 1100 nm we see oscillations which signifies that there is some interaction between aluminium and TCO. The wavelength is not long enough to make free carrier absorption happen which is below the bandgap of TCO.

At 1600 nm we see the reflectance to be 0 which is related to the plasma wavelength. At this point, all the carriers are absorbing light so there is no reflection as in plasma wavelength the metal starts to be opaque. After 1600 nm there is absorption by the free carriers.

These curves can be fitted using a parameter called Tauc-Lorentz energy and by using this we can estimate the thickness of the TCO which is out of scope for this thesis. As for different TCO, the oscillations will be different, and the resulting thickness is called optical thickness.

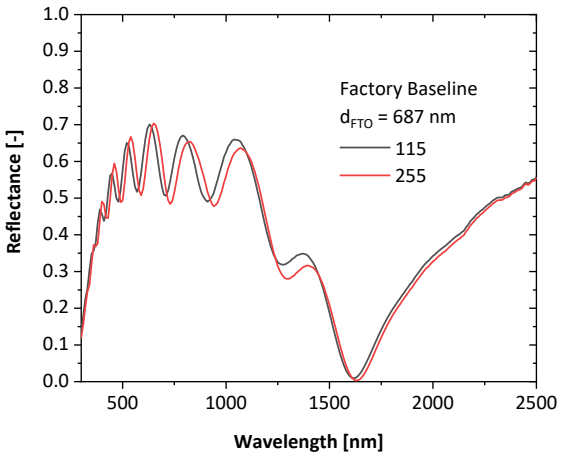

Figure 4. 35: Difference in CoM Factory baseline

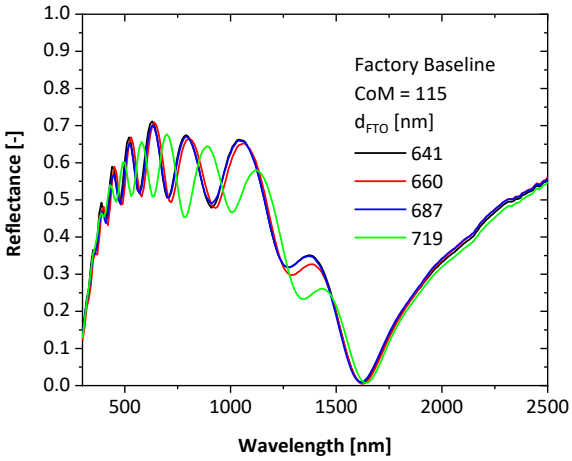

Figure 4. 36: Difference in TCO thickness-Factory baseline

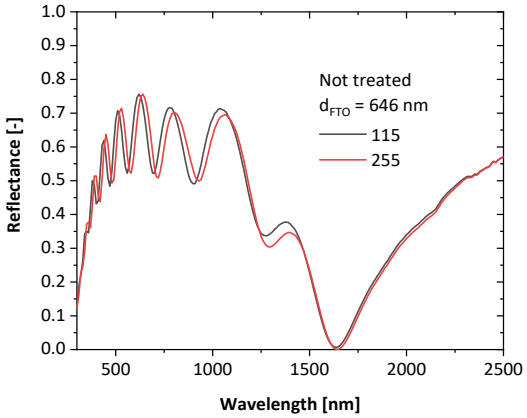

Figure 4. 37: Difference in CoM- Not treated samples

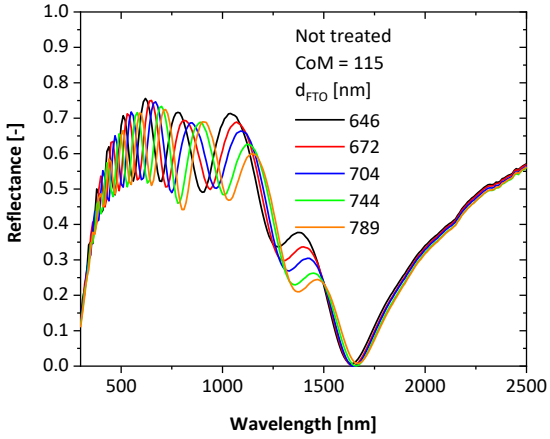

Figure 4. 38: Difference in TCO thickness-Not treated samples

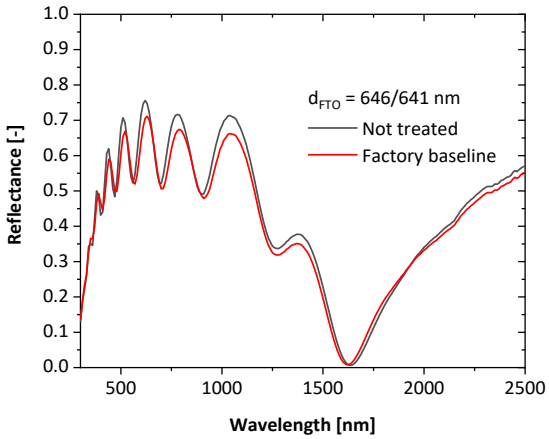

Figure 4. 39: Comparison between not treated and factory baseline samples

4.5. TCO + Carrier foil-based samples:

4.5.1. Structural Characterization using 3D Confocal Microscope:

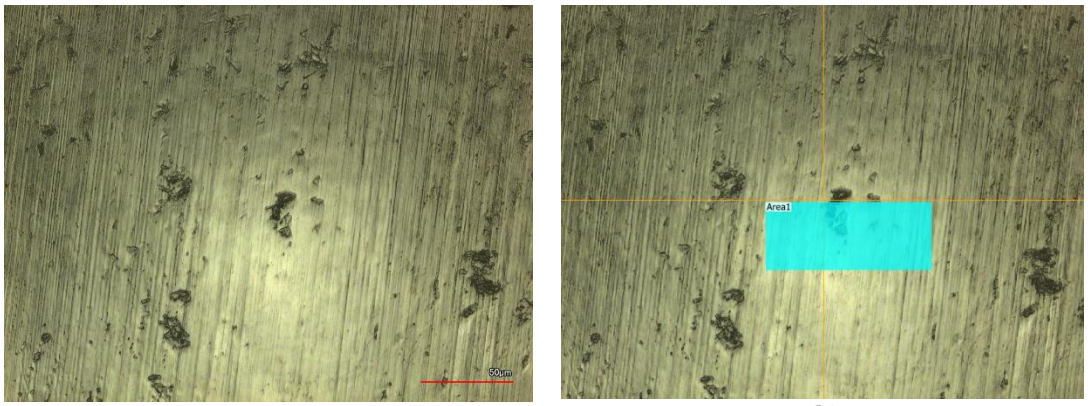

(a) (b)

Figure 4. 40: 3D confocal images of (a) TCO + Carrier foil (b) Area to be characterized

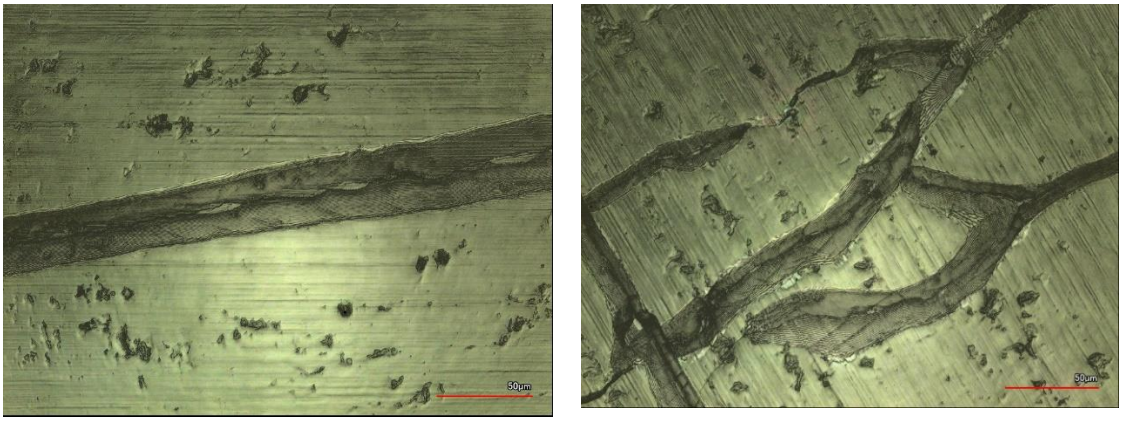

Figure 4. 41: 3D confocal images showing damages to the TCO + Carrier foil

Figure 4.40 above shows the 3D confocal images of the TCO + Carrier foil. One major problem while handling these foils is that you must cut the sample to characterize them under the microscope. These are sensitive foils and develop cracks that propagate further. So, in figure 4.41 we can see these cracks that look like milling tracks. While measuring the roughness parameters in the software these cracks give a higher value which isn't the true roughness characteristic of the carrier foil.

Below is figure 4.42, 4.43, and 4.44 are the graphs showing the comparison between various roughness parameters of Sa, Sz, and Spc with TCO + Carrier foil with varying thicknesses. Initially, there is an increase in the roughness values, and with an increase in TCO thickness, the roughness decreases and remains almost the same.

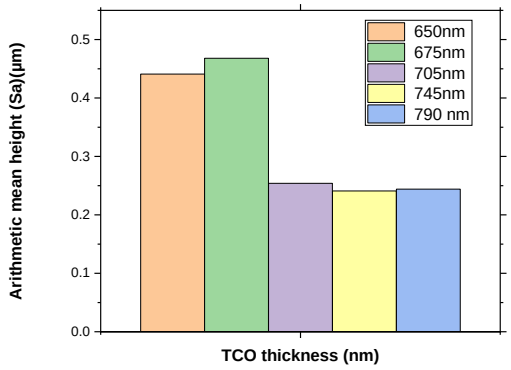

Figure 4. 42: Arithmetic mean height for TCO + Carrier foil

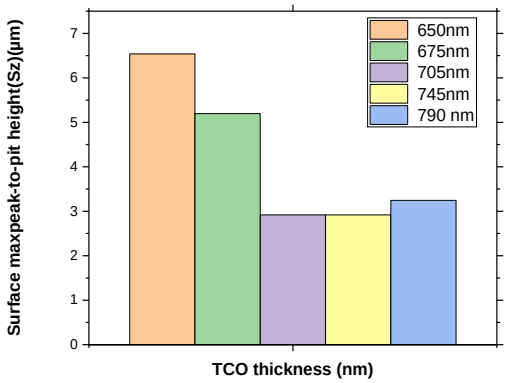

Figure 4. 43: Surface max peak-to-pit height for TCO + Carrier foil

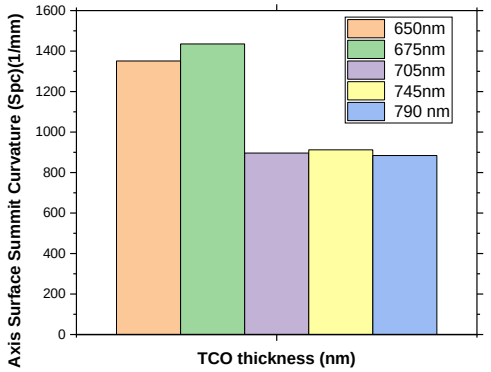

Figure 4. 44: Axis surface summit curvature for TCO + Carrier foil

4.5.2. Structural Characterization using SEM:

Figure 4.45 below shows the SEM image of baseline TCO + Carrier foil in which there is a milling track of thickness 4.8214 μm. Milling tracks are not found much in this set of samples. One problem which was discussed in the previous section would be the handling of the foil. As these foils are sensitive it develops cracks that develop further as seen in Figures 4.46 and 4.47 so which makes it difficult to properly characterize them.

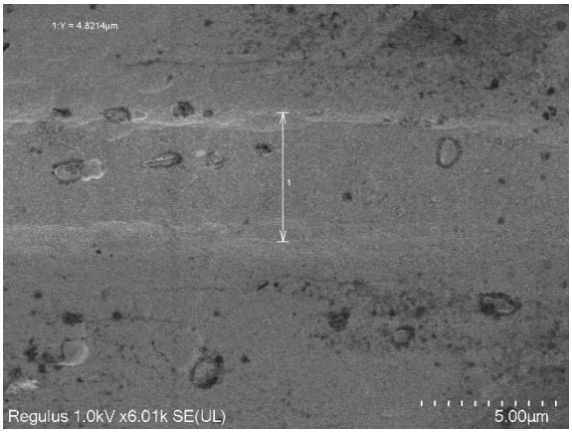

Figure 4. 45: SEM image of baseline carrier foil with TCO

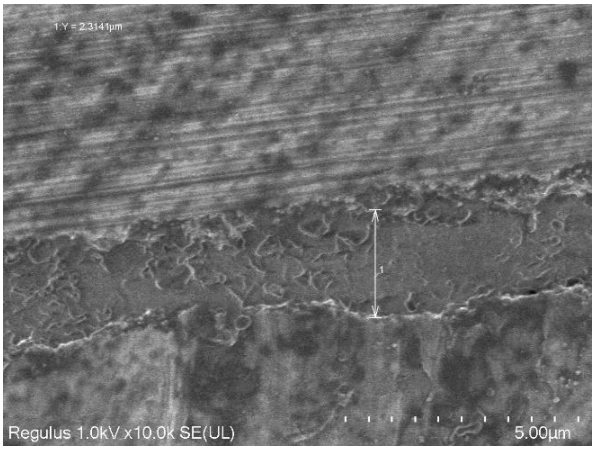

Figure 4. 46: SEM image of TCO + Carrier foil with TCO thickness of 650nm

Figure 4. 47: SEM image of TCO + Carrier foil with cracks

4.5.3. Optical Characterization using Spectrophotometer:

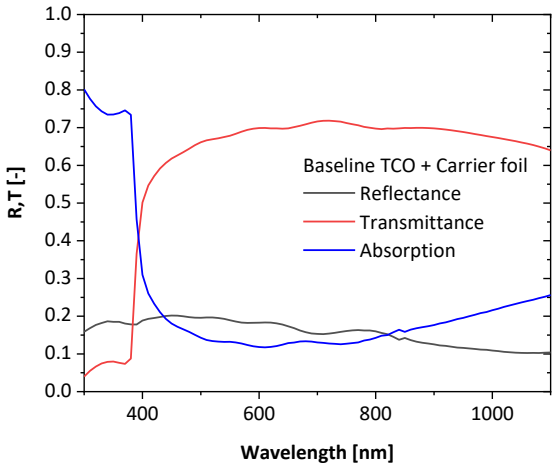

Figure 4. 48: Optical characterization of carrier foil with baseline TCO

The optical properties measured using the integrating sphere for the baseline TCO with carrier foil are shown in figure 4.48. As the carrier foil is transparent, we can see the reflectance is almost 15% which is low as most of the light passes away and the transmittance through the foil is 55% in the visible wavelength which is quite good. Absorption here is total absorption as both TCO and the carrier foil are absorbing the light. In the visible spectrum, the absorption is 10% and for the UV spectrum, it increases to 80% this is because of the bandgap of the TCO. If there would have been glasses as the substrate instead of carrier foil the absorption graph in the UV range would have been lower and we could have seen absorption only by TCO.

4.5.4. Electrical Characterization using Hall Effect Measurement:

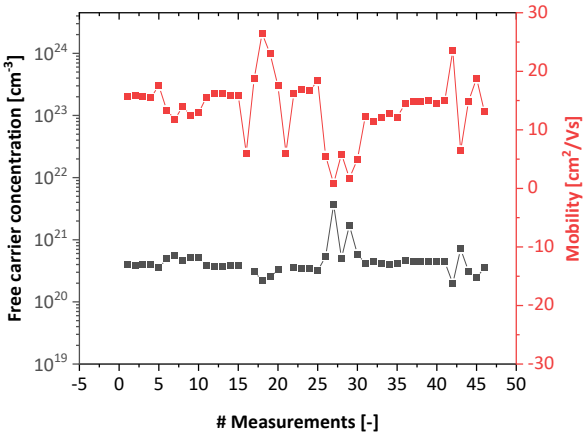

Figure 4. 49: Electrical characterization using hall effect setup for Baseline TCO + Carrier foil

For electrical characterization, we use the hall effect measurement that gives us the mobility and free carrier concentration of the carrier foil. Initially, for measurement, one piece per foil was used but that gave results that were not comparable. To get uniform results each foil was divided into 5 (1x1cm^2) pieces and there was a total of 9 foils. Some samples don't show us uniformity in measurement as seen in figure 4.49. But most of the samples have free carrier concentration between 3.3 x 10^{20} cm^{-3} to 4 x 10^{20} cm^{-3} and mobility of 13 cm^2/Vs to 15 cm^2/Vs. A low free carrier concentration and high mobility are needed for less optical loss to reach high conductivity and high transparency.

5

Conclusion

This thesis focussed on the analysis and surface characterization of bare aluminium foils, textured aluminium foils, TCO + Al foils, and TCO + carrier foils. Various methods involving morphological, optical, and electrical characterization were performed.

Round robin experiment performed on bare aluminium foil to find out which measurement technique is best suited for HyET solar. The pre-treated sample had higher roughness values compared to the untreated and annealed samples. From this set of experiments, it was found out that results found at TU Delft using a 3D Confocal microscope provided a good correlation with one of the companies.

Morphological analysis was done using 3D Confocal Microscope and Scanning Electron Microscope. For textured aluminium foils 2020 untreated and baseline samples, 2021 untreated, and baseline samples were used. More milling tracks and rough morphology were found in the 2020 baseline samples compared to the 2021 baseline samples. From the SEM imaging, the milling tracks were confirmed, and we see the presence of precipitants in the pre-treated samples that further cause problems in the TCO deposition. In the untreated samples, the major problem was milling tracks and pinholes. FLAM02 textured samples compared to the 2020 factory baseline and 2021 factory baseline showed a higher value in roughness. This has a better impact on the optical properties of the foil. Also, doing the SEM imaging we can see that the milling tracks are missing as in this texturing a good amount of aluminium is etched away. Precipitants are the only issue remaining. From the AFM analysis done for the FLAM02 textures, the overall RMS roughness was found to be 161.3 nm, autocorrelation length to be 1.36 μm and the aspect ratio to be 11.8%.

For Al + TCO samples when characterized in a 3D confocal microscope a higher value of roughness was noticed in the pre-treated samples compared to the untreated samples. Baseline pre-treated samples showed the presence of milling tracks and precipitants in SEM imaging. In untreated samples, islands of TCO were noticed as well. The optical thickness of TCO was checked using SEM for different thicknesses of 650 nm, 675 nm, 705 nm, 745 nm, and 790 nm. The thickness from the SEM was found to be 656.7 nm, 671.8 nm, 700.46 nm, 740.11 nm, 785.16 nm.

The TCO + Carrier foil when characterized through a 3D confocal microscope initially shows an increase in roughness value and then the roughness decreases and remains almost the same. Fewer milling tracks were noticed in the SEM imaging. These samples must be cut to characterize them and as they are sensitive, we could see a lot of cracks in the sample in both 3D confocal and SEM imaging.

Optical characterization was done using a Spectrophotometer with Integrating Sphere. For the textured samples, both the 2020 and 2021 factory baseline have similar values in the diffused reflectance and the 2020 factory baseline has a bit higher value in specular reflectance. For

FLAM02 textured samples diffused reflectance was higher compared to the 2021 factory baseline and FLAM01 textures. Haze values for FLAM02 samples were also higher compared to FLAM01 and factory baseline**.** In TCO + Al foils we see oscillations between 400 nm to 1100 nm showing the interaction between aluminium and TCO with a similar trend for all the samples. For TCO + Carrier foils reflectance is around 15 % and transmittance of 55 % as the foils are transparent. Here total absorption is considered as both TCO and carrier foil is absorbing light. In the visible spectrum, the absorption is 10% which increases to 80% in the UV region because of the bandgap of TCO.

Finally, electrical characterization is done on TCO + Carrier foil using Hall Effect Measurement as they are non-conducting. The free carrier concentration was found to be between 3.3 x 10^{20} cm^{-3} to 4 x 10^{20} cm^{-3} and mobility of 13 cm^2/Vs to 15 cm^2/Vs. A low free carrier concentration and high mobility are needed for less optical loss to reach high conductivity and high transparency.

6

Recommendations

Some recommendations that can be given based on this thesis for future works are:

While making the roughness characterization using Sz it can be defined using two separate variables that can be measured using a 3D confocal microscope. The reference plane instead of being set at the zero point can be set at the middle plane of the foil. From the zero point to the positive value, it can give the maximum height which will give the data on milling tracks and precipitants. For zero point to the negative value, we can get the roughness value on the holes.

For FLAM02 textured surface, there are no devices made as TCO has not been optimized to be deposited on them. In FLAM01 textured foils when it was deposited with TCO all the devices were shunted. If TCO deposition on FLAM02 is done successfully one major issue that foils deal with is milling tracks and pinholes can be eliminated. Then rather than specified on the company for characterizing the foils, HyET solar can do that by FLAM02 texturing.

As precipitants are one major issue in the pre-treated samples, they can be treated with different acids like nitric acid and phosphoric acid to see if they help in reducing the precipitant concentration or eliminating them.

While handling the TCO + Carrier foil sample we can see cracks in the sample after cutting them as the foils are sensitive. So, a better way has to be found out on how to take smaller pieces of sample for characterization as with cracks it affects the roughness measurements.

The leak test is a characterization test that can be performed on the samples to check the resistance of the TCO.

Bibliography

1. Energy Alabama, (2019), "What is Sustainable Energy?" [Online]. Availab1e: https://alcse.org/energy-alabama/our-work/education/what-is-sustainable-energy/
2. IEA, Renewable electricity generation increase by technology, 2019-2020 and 2020-2021, IEA, Paris https://www.iea.org/data-and-statistics/charts/renewable-electricity-generation-increase-by-technology-2019-2020-and-2020-2021
3. IEA, (Jan 10, 2022), "Solar" [Online]. Available: https://www.iea.org/fuels-and-technologies/solar
4. SolarPower Europe, (July 20, 2021), "Cumulative installed solar PV capacity worldwide from 2000 to 2020 (in megawatts)" [Graph]. In Statista. Available: https://www.statista.com/statistics/280220/global-cumulative-installed-solar-pv-capacity/
5. Efaz, E. T., Rhaman, M. M., Al Imam, S., Bashar, K. L., Kabir, F., Sakib, S. N., & Mourtaza, M. E. (2021). A review of major technologies of thin-film solar cells. Engineering Research Express.
6. Lee, T. D., & Ebong, A. U. (2017). A review of thin film solar cell technologies and challenges. Renewable and Sustainable Energy Reviews, 70, 1286-1297.
7. American Solar Energy Society, (February 27, 2021), "Thin-Film Solar Panels" [Online]. Available: https://ases.org/thin-film-solar-panels/
8. A. V. Shah, H. Schade, M. Vanecek, J. Meier, E. Vallat-Sauvain, N. Wyrsch, U. Kroll, C. Droz, and J. Bailat, "Thin-film silicon solar cell technology," Progress in Photovoltaics: Research and Applications, vol. 12, no. 2-3, pp. 113–142, 2004.
9. T. D. Lee and A. U. Ebong, "A review of thin film solar cell technologies and challenges," Renewable and Sustainable Energy Reviews, vol. 70, pp. 1286–1297, 2017.
10. J. Poortmans and V. Arkhipov, Thin Film Solar Cells: Fabrication, Characterization and Applications. JohnWiley & Sons, 2006, vol. 18.
11. Soppe, W. J., Van Aken, B. B., Dörenkämper, M., Devilee, C., Heijna, M. C. R., & Löffler, J. (2009, September). Roll to roll fabrication process of thin-film silicon solar cells on steel foil. In Proc. 24th European Photovoltaic Solar Energy Conf. and Exhibition (Hamburg, Germany, 21–25th September 2009) (pp. 2750-2753).
12. R. Søndergaard, M. Hösel, D. Angmo, T. T. Larsen-Olsen, and F. C. Krebs, "Roll-to-roll fabrication of polymer solar cells," *Materials Today*, vol. 15, no. 1-2, pp. 36–49, 2012. [Online]. Available: http://dx.doi.org/10.1016/S1369-7021(12)70019-6
13. HyET Solar, (2022), "Thin film production process,". [Online]. Available: https://www.hyetsolar.com/ production-process/
14. Hyet Solar, (2022), "Thin film technology,". [Online]. Available: https://www.hyetsolar.com/technology/Thin-Film-Solar/
15. *Flexible Lightweight Advanced Materials In Next Generation Of PV: FlamingoPV*. Project Description, Delft University of Technology and HyET Solar, August 2018.
16. R. Schropp, E.Middelman, E. Andel, van, H.Meiling, C.Werf, van der, P. Peters, L. Jonge-Meschaninova, de, J.Winkeler, R. Severens, M. Zeman, M. Sanden, van de, A. Kuijpers, C. Spee, and G. Jongerden, "Novel superstrate process for textured sno2:f/p+-i-n+ amorphous silicon solar cells suitable for rol-to-roll deposition," in *Proceedings of the 2nd World Conference on Photovoltaic Solar Energy Conversion, Vienna, 6-10 July 1998*, 1998, 2ndWorld Conference on Photovoltaic Solar Energy Conversion ; Conference date:06-07-1998 Through 10-07-1998.
17. Nawaratne, S. (2020). Nanocrystalline Silicon Solar Cells on Flexible Al Substrates.

18. Smets, A. H., Jäger, K., Isabella, O., Swaaij, R. A., & Zeman, M. (2015). *Solar Energy: The physics and engineering of photovoltaic conversion, technologies and systems*. UIT Cambridge.
19. Hussain, C. M. (Ed.). (2018). *Handbook of nanomaterials for industrial applications*. Elsevier.
20. ODTU GUNAM, (2015), "What are the PV cell types?" [Online]. Available: http://gunam.metu.edu.tr/solar-tech/pv-cell-types/
21. GCell, (2022), "Solar Cells" [Online]. Available: https://gcell.com/knowledge-hub/solar-cells
22. Sino Voltaics, (2022), "Surface Tecturing" [Online]. Available: https://sinovoltaics.com/learning-center/basics/surface-texturing/
23. Shah, A. M. (2021). Optimization of modulated surface texturing for flexible thin-film silicon solar cells.
24. Isabella, O., Krč, J., & Zeman, M. (2010). Modulated surface textures for enhanced light trapping in thin-film silicon solar cells. *Applied Physics Letters*, *97*(10), 101106.
25. Tan, H., Moulin, E., Si, F. T., Schüttauf, J. W., Stuckelberger, M., Isabella, O., ... & Smets, A. H. (2015). Highly transparent modulated surface textured front electrodes for high-efficiency multijunction thin-film silicon solar cells. *Progress in Photovoltaics: Research and Applications*, *23*(8), 949-963.
26. Nasuno, Y., Kondo, M., & Matsuda, A. (2001). Effects of substrate surface morphology on microcrystalline silicon solar cells. *Japanese Journal of Applied Physics*, *40*(4A), L303.
27. Tan, H., Psomadaki, E., Isabella, O., Fischer, M., Babal, P., Vasudevan, R., ... & Smets, A. H. (2013). Micro-textures for efficient light trapping and improved electrical performance in thin-film nanocrystalline silicon solar cells. *Applied Physics Letters*, *103*(17), 173905.
28. Python, M., Vallat-Sauvain, E., Bailat, J., Dominé, D., Fesquet, L., Shah, A., & Ballif, C. (2008). Relation between substrate surface morphology and microcrystalline silicon solar cell performance. *Journal of Non-Crystalline Solids*, *354*(19-25), 2258-2262.
29. AZO NANO, (2022), "Regulus8230: A High Resolution Scanning Electron Microscope." [Online]. Available: **https://www.azonano.com/equipment-details.aspx?EquipID=1866**
30. Hitachi, (2022), "Ultra-high Resolution Scanning Electron Microscope Regulus Series." [Online]. Available: https://www.hitachi-hightech.com/global/science/products/microscopes/electron-microscope/fe-sem/regulus.html
31. C. Woodford, (2022), "Electron microscopes" [Online]. Available: https://www.explainthatstuff.com/electronmicroscopes.html
32. Stanford Nano Shared facilities, (2022), "Microscopy: Keyence VK-X250 3D Laser Scanning Confocal Microscope." [Online]. Available: https://snsf.stanford.edu/facilities/fab/npc/keyence
33. Keyence,(2022) "3D Laser scanning microscope - VK-X250," [Online]. Available: https://www.keyence.com/landing/microscope/lp_vk250_micro.jsp
34. L. Zhao and I. K. Jäger, "Enhancement of light trapping in thin film silicon solar cells," 2009.
35. D. Rajagopal and P. Materials, "Modulated Surface Texturing on Temporary Aluminium Substrate for
Flexible Thin-Film Solar Cells A FlamingoPV project Modulated Surface Texturing on Temporary Aluminium Substrate for Flexible Thin-Film Solar Cells A FlamingoPV project," Tech. Rep. July, 2020.
36. S. Elzwawi, "Cathodic arc zinc oxide for active electronic devices," 2015.
37. Ge, H. (2017). Development of High Efficiency SHJ/Poly-Si Passivating Contact Hybrid Solar Cells.
38. Keyence, (2022), "Area Roughness parameters." [Online]. Available: https://www.keyence.com/ss/products/microscope/roughness/surface/parameters.jsp

Appendix

A.1.Round Robin Samples Roughness Characterization:

Samples	Surface max peak-to-pit height (Sz)(µm)
2011(Untreated)2011(Untreated)	0.17252
2020(Pre-treated)2020(Pre-treated)	2.92242
2020(Un-treated)2020(Un-treated)	0.49013
2020(Annealed)2020(Annealed)	0.31693
2020(Annealed + Pre-treated)	2.52316

Table A. 1: Surface max peak-to-pit height for different samples

Samples	Surface Summit Curvature (Spc)(1/mm)
2011(Untreated)2011(Untreated)	26.8791
2020(Pre-treated)2020(Pre-treated)	942.644
2020(Un-treated)2020(Un-treated)	89.3442
2020(Annealed)2020(Annealed)	112.853
2020(Annealed + Pre-treated)	376.052

Table A. 2: Surface Summit Curvature for different samples

A.2. Baseline Textured Samples Roughness Characterization:

Samples	Arithmetic mean height (Sa)(µm)
Untreated 2020	0.129
Untreated 2021	0.082
Factory Baseline 2020	0.528
Factory Baseline 2021	0.165

Table A. 3: Arithmetic mean height for baseline textured samples

Samples	Surface max peak-to-pit height (Sz)(µm)
Untreated 2020	3.446
Untreated 2021	3.888
Factory Baseline 2020	9.733
Factory Baseline 2021	5.87

Table A. 4: Surface max peak-to-pit height for baseline textured samples

Samples	Axis Surface Summit Curvature (Spc)(1/mm)
Untreated 2020	1068.396
Untreated 2021	1440.244
Factory Baseline 2020	8306.811
Factory Baseline 2021	5477.472

Table A. 5: Axis Surface Summit Curvature for baseline textured samples

A.3. FLAM02 Textured Sample Roughness Comparison:

Samples	Arithmetic mean height (Sa)(µm)
2020 Factory baseline	0.442
FLAM02	0.948
2021 Factory Baseline	0.23

Table A. 6: Arithmetic mean height for FLAM02 textured samples

Samples	Surface max peak-to-pit height (Sz)(µm)
2020 Factory baseline	12.252
FLAM02	14.485
2021 Factory Baseline	6.927

Table A. 7: Surface max peak-to-pit height for FLAM02 textured samples

Samples	Axis Surface Summit Curvature (Spc)(1/mm)
2020 Factory baseline	9778.097
FLAM02	21163.925
2021 Factory Baseline	5477.472

Table A. 8: Axis Surface Summit Curvature for FLAM02 textured samples

A.4. Al + TCO Based Samples Roughness Characterization:

TCO thickness (nm)	Arithmetic mean height (Sa)(µm) (Untreated Samples)	Arithmetic mean height (Sa)(µm) (Pre-treated Samples)
650	0.262	0.258
675	0.118	0.204
705	0.161	0.248
745	0.126	0.193

Table A. 9: Arithmetic mean height for Al + TCO untreated and pre-treated samples

TCO thickness (nm)	Surface max peak-to-pit height (Sz)(µm) (Untreated Samples)	Surface max peak-to-pit height (Sz)(µm) (Pre-treated Samples)
650	6.788	9.881
675	4.354	6.412
705	3.276	1.934
745	8.719	9.091

Table A. 10: Surface max peak-to-pit height for Al + TCO untreated and pre-treated samples

TCO thickness (nm)	Axis Surface Summit Curvature (Spc)(1/mm) (Untreated Samples)	Axis Surface Summit Curvature (Spc)(1/mm) (Pre-treated Samples)
650	5282.615	10307.472
675	1799.749	5885.322
705	3699.774	9489.321
745	4225.347	3788.796

Table A. 11: Axis Surface Summit Curvature for Al + TCO untreated and pre-treated samples

A.5. TCO + Carrier Foil Based Samples Roughness Characterization:

TCO thickness (nm)	Arithmetic mean height (Sa)(µm)
650	0.441
675	0.468
705	0.254
745	0.241
790	0.244

Table A. 12: Arithmetic mean height for TCO + Carrier foil samples

TCO thickness (nm)	Surface max peak-to-pit height (Sz)(µm)
650	6.54
675	5.197
705	2.919
745	2.919
790	3.246

Table A. 13: Surface max peak-to-pit height for TCO + Carrier foil samples

TCO thickness (nm)	Axis Surface Summit Curvature (Spc)(1/mm)
650	1351.165
675	1435.241
705	896.176
745	912.187
790	884.274

Table A. 14: Axis Surface Summit Curvature for TCO + Carrier foil samples